

Recent ground thermo-hydrological changes in a Southern Tibetan endorheic catchment and implications for lake level changes

Léo C.P. Martin^{1,2,3}, Sebastian Westermann^{2,4}, Michele Magni¹, Fanny Brun^{1,5}, Joel Fiddes⁶, Yanbin Lei^{7,8}, Philip Kraaijenbrink¹, Tamara Mathys⁹, Moritz Langer^{10,11}, Simon Allen¹² and Walter W. Immerzeel¹

1. Faculty of Geosciences, Utrecht University, Utrecht, The Netherlands
2. Department of Geosciences, University of Oslo, Blindern, 0316 Oslo, Norway
3. Aix Marseille Univ, CNRS, IRD, INRAE, CEREGE, Aix-en-Provence, France
4. Center for Biogeochemistry in the Anthropocene, Oslo, Norway
5. Université Grenoble Alpes, CNRS, IRD, Grenoble INP, IGE, Grenoble, France
6. WSL Institute for Snow and Avalanche Research SLF, Davos, Switzerland
7. Key Laboratory of Tibetan Environment Changes and Land Surface Processes, Institute of Tibetan Plateau Research, Chinese Academy of Sciences, Beijing 100101, China
8. CAS Center for Excellence in Tibetan Plateau Earth System Sciences, Beijing 100101, China
9. Department of Geosciences, University of Fribourg, Fribourg, Switzerland
10. Alfred Wegener Institute Helmholtz Centre for Polar and Marine Research, 14473 Potsdam, Germany
11. Department of Geography, Humboldt Universität zu Berlin, 12489 Berlin, Germany
12. Department of Geography, University of Zurich, Zürich, Switzerland

Correspondence to: Léo Martin (leo.doug.martin@gmail.com)
Walter Immerzeel (w.w.immerzeel@uu.nl)

Abstract: 418 words
Main: 13,364 words, 11 figures, 2 tables
Appendices: 446 words, 3 figures, 1 table

a supprimé: 401

a supprimé: 12,426

a supprimé: 1 table

a supprimé: 441

Abstract

Climate change modifies the water and energy fluxes between the atmosphere and the surface in mountainous regions such as the Qinghai-Tibet Plateau (QTP), which has shown substantial hydrological changes over the last decades, including rapid lake level variations. The ground across the QTP hosts either permafrost or seasonally frozen and, in this environment, the ground thermal regime influences liquid water availability, evaporation and runoff. Therefore, climate-driven modifications of the ground thermal regime may contribute to lake level variations, yet this hypothesis has been relatively overlooked until now.

This study focuses on the cryo-hydrology of the catchment of Lake Paiku (Southern Tibet) for the 1980-2019 period. We use TopoSCALE and TopoSUB to downscale ERA5 data, in an effort to account for the spatial variability of the climate in our forcing data. We use a distributed setup of the CryoGrid community model (version 1.0) to quantify thermo-hydrological changes in the ground during this period. Forcing data and simulation outputs are validated with data from a weather station, surface temperature loggers and observations of lake level variations. Our lake budget reconstruction shows that the main water input to the lake is direct precipitation (310 mm per year), followed by glacier runoff (280 mm per year) and land runoff (180 mm per year). However, altogether these components do not offset evaporation (860 mm per year).

Our results show that both seasonal frozen ground and permafrost have warmed (0.17 °C per decade 2 m deep), increasing the availability of liquid water in the ground and the duration of seasonal thaw. Correlations with annual values suggest that both phenomena promote evaporation and runoff. Yet, ground warming drives a strong increase in subsurface runoff, so that the runoff/(evaporation + runoff) ratio increases over time. This increase likely contributed to stabilizing the lake level decrease after 2010.

Summer evaporation is an important energy sink and we find active layer deepening only where evaporation is limited. The presence of permafrost is found to promote evaporation at the expense of runoff, consistent with recent studies suggesting that a shallow active layer maintains higher water contents close to the surface. However, this relationship seems to be climate-dependent and we show that a colder and wetter climate produces the opposite effect. Although the present study was performed at catchment scale, we suggest that this ambivalent influence of permafrost may help to understand the contrasting lake level variations observed between the South and North of the QTP, opening new perspectives for future investigations.

a supprimé: . This is particularly true over

a supprimé: a major headwater region of the world,

a supprimé: . Among them, the

a supprimé: observed throughout the plateau remain puzzling, and much is still to be understood regarding the spatial distribution of lake level trends (increase/decrease) and paces.

a supprimé: ground and both are affected by climate change. In

a supprimé: . For now,

a supprimé: by modelers because of the scarcity of field data and the difficulty to account for the spatial variability of the climate and its influence on the ground thermo-hydrological regime in a numerical framework

a supprimé: and capture

a supprimé: the

a supprimé: data

a supprimé: logger data

a supprimé: We

a supprimé: .

a supprimé:

a supprimé: This

a supprimé: south

a supprimé: north

53 Main text

54 1. Introduction

55 Climate change is amplified in mountainous environments, with major consequences for
56 ecosystems, landscapes, hydrology, human communities and infrastructure (IPCC, 2019). Station
57 observations show that global warming is elevation dependent, with the strongest warming rates being
58 observed at high elevations (Pepin et al., 2015; Wang et al., 2014). Over the Qinghai-Tibet Plateau
59 (QTP), a significant increase in surface air temperatures has been recorded since the 1980s, in particular
60 in the North of the plateau (Zhang et al., 2022). This has been accompanied by a decrease in wind speed,
61 humidification of the air, and a general increase in precipitation, although with a strong spatial
62 variability (Bibi et al., 2018). Altogether, these changes have affected the surface energy balance of the
63 plateau through a shift of the Bowen ratio towards more latent heat fluxes, limiting the sensible surface
64 warming (Yang et al., 2014a).

65 These changes in water and energy fluxes between the atmosphere and the surface have the potential
66 to alter the hydrological cycle of the QTP, which is the headwater region for major Asian rivers. As
67 such, increasing trends of evaporation over land have been measured (3.8 mm per decade since the
68 1960s) with strong spatial variability both in absolute values and increase rates (Wang et al., 2020b).
69 Changes in the seasonality of river discharge (Cao et al., 2006) and groundwater discharge (Niu et al.,
70 2011) were reported for the same period. Overall glacier shrinkage has also been observed since the
71 1960s with a persistent increase in glacier mass loss rates (Bhattacharya et al., 2021; Hugonnet et al.,
72 2021).

73 The QTP also features more than 1,000 lakes larger than 1 km² (Zhang et al., 2017), most of them
74 located in endorheic catchments. Lake volume changes are therefore attributable to climatic and
75 hydrological changes occurring within the lake catchment, such as glacier melt, ground ice melt,
76 precipitation, evaporation or runoff patterns. The majority of these lakes have experienced a pronounced
77 increase in water levels since the 1990s (Lei et al., 2013, 2014), a trend that was suggested to be mainly
78 driven by changes in precipitation and evaporation patterns (Yao et al., 2018) rather than by an increase

a supprimé: Climate change is amplified in mountainous environments, with major consequences for ecosystems, landscapes, hydrology, human communities and infrastructure (IPCC, 2019). Station observations show that global warming is elevation dependent, with the strongest warming rates being observed at high elevations (Pepin et al., 2015; Wang et al., 2014). Over the Qinghai-Tibet Plateau (QTP), a significant increase in surface air temperatures has been recorded since the 1980s, in particular in the North of the plateau (Zhang et al., 2022 and references therein). It is accompanied by a decrease in wind speed, humidification of the air, and a general increase in precipitation, but with a strong spatial variability (Bibi et al., 2018). Altogether, these changes have affected the surface energy balance of the plateau through a shift of the Bowen ratio towards more latent heat fluxes, limiting the sensible surface warming (Yang et al., 2014a).¶

These changes in water and energy fluxes between the atmosphere and the surface have the potential to alter the hydrological cycle of the QTP, which is the headwater region for major Asian rivers. As such, increasing trends of evaporation over land have been measured (3.8 mm per decade since the 1960s) with strong spatial variability both in absolute values and increase rates (Wang et al., 2020b). Changes in the seasonality of river discharge (Cao et al., 2006) and groundwater discharge (Niu et al., 2011) were reported for the same period. Overall glacier shrinkage is also observed since the 1960s with a persistent increase in glacier mass loss rates (Bhattacharya et al., 2021).¶

The QTP also features more than 1,000 lakes larger than 1 km² (Zhang et al., 2017), most of them located in endorheic catchments. Lake volume changes are therefore attributable to climatic and hydrological changes occurring within the lake catchment, such as glacier melt, ground ice melt, precipitation, evaporation or runoff patterns. A majority of these lakes have experienced a pronounced increase in water levels since the 1990s (Lei et al., 2013, 2014), a trend that was suggested to be mainly driven by changes in precipitation and evaporation patterns (Yao et al., 2018) rather than by an increase in glacier mass loss (Brun et al., 2020). Nevertheless, lake level variations are not uniform across the QTP and exhibit important spatial variability. Whereas the northern and central QTP have recorded lake expansion, the southern parts of the plateau have experienced lake shrinkage (Qiao et al., 2019; Zhang et al., 2020, 2021a). Such a complex pattern challenges our understanding of the hydrological changes occurring in these high Asian watersheds.¶

In this regard, new insights on hydroclimatic changes over the QTP can emerge from the investigation of the coupled energy and water fluxes between the ground surface/subsurface and the atmospheric boundary layer. These fluxes are driven by the climate and have a major impact on cold-region hydrology (Bring et al., 2016; Gao et al., 2021; Pomeroy et al., 2007). Indeed, hydrological variables (precipitation, evaporation, runoff) affect the soil water content, which changes its thermal properties, the distribution between latent and sensible fluxes and thus substantially influences the ground thermal regime (Bring et al., 2016; Koren et al., 1999; Martin et al., 2019). In turn, the ground thermal regime modifies the relative proportion of frozen and liquid subsurface water, influencing infiltration possibilities and the amount of water available for evaporation and surface/subsurface runoff (Carey and Woo, 2001; Yi et al., 2006). So far, climate induced thermo-hydrological changes over the QTP have received limited attention. Large-scale modeling studies reported changes in the seasonal ground freezing cycles characterized by a reduction of the frost def

227 in glacier mass loss and runoff (Brun et al., 2020; Zhang et al., 2021a). Nevertheless, lake level
228 variations are not uniform across the QTP and exhibit important spatial variability. Whereas the
229 northern and central QTP have recorded lake expansion, the southern parts of the plateau have
230 experienced lake shrinkage (Qiao et al., 2019; Zhang et al., 2021a, 2020a). Such a complex pattern
231 challenges our understanding of the hydrological changes occurring in these high Asian watersheds.

232 In this regard, new insights on hydroclimatic changes over the QTP can emerge from the
233 investigation of the coupled energy and water fluxes between the ground surface/subsurface and the
234 atmospheric boundary layer. These fluxes are driven by the climate and have a major impact on cold-
235 region hydrology (Pomeroy et al., 2007; Gao et al., 2021; Bring et al., 2016). Indeed, hydrological
236 variables (precipitation, evaporation, runoff) affect the soil water content, which changes its thermal
237 properties, the distribution between latent and sensible fluxes and thus substantially influences the
238 ground thermal regime (Bring et al., 2016; Koren et al., 1999; Martin et al., 2019). In turn, the ground
239 thermal regime modifies the relative proportion of frozen and liquid subsurface water, influencing
240 infiltration possibilities and the amount of water available for evaporation and surface/subsurface runoff
241 (Yi et al., 2006; Carey and Woo, 2001).

242 So far, climate induced thermo-hydrological changes over the QTP have received limited attention.
243 Large-scale modeling studies reported changes in the seasonal ground freezing cycles characterized by
244 a reduction of the frost depth and duration of the frozen period since the 1960s (Qin et al., 2018; Wang
245 et al., 2020a) and notable ground warming trends in summer and winter (Qin et al., 2021). Similar
246 ground warming trends were reported in the regional modeling study from Qin et al. (2017), along with
247 an increasing trend in evaporation and a decrease of the runoff coefficient over time. Plateau-scale
248 surface energy balance modeling from Wang et al. (2020b) reported that increasing trends in
249 evapotranspiration could be mainly explained by variations in air temperature and net radiation at the
250 surface.

251 Complementary to seasonally frozen ground, permafrost is also a distinctive feature of climate-
252 surface interactions in cold regions. Large-scale permafrost modeling suggests that it covers a
253 significant part of the QTP, mainly as continuous permafrost in the north of the plateau and as
254 discontinuous or sporadic in the south (Obu et al., 2019). Permafrost on the QTP usually has a low ice

255 content due to limited precipitation and strong evaporation (Wu et al., 2005; Yang et al., 2010).
256 Borehole temperature measurements show that it is a relatively warm type of permafrost (Biskaborn et
257 al., 2019; Wu and Zhang, 2008) and its exposure to high solar radiations makes it sensitive to changes
258 in surface conditions and climate change (Yang et al., 2010). Since the 1960s, climate change has driven
259 permafrost warming across the plateau (Ran et al., 2018; Shaoling et al., 2000). Ran et al. (2018) reports
260 that most of the plateau exhibits a warming trend of the ground comprised between 0.26 and 0.74 °C
261 per decade and half of the plateau warms at a rate higher than 0.5 °C per decade. This warming is
262 accompanied by upward migration (of around 100 m between the 1960s and 2000s) and shrinkage of
263 permafrost covered areas (24% of the permafrost extent lost between the 1960s and the 2000s, Ran et
264 al., 2018).

265 Permafrost grounds are characterized by a strong interplay between the ground thermal regime and
266 the land hydrology. Seasonal thawing and freezing of the active layer are driven by the surface energy
267 balance which, in return, influences surface and subsurface runoff (Kurylyk et al., 2014; Walvoord and
268 Kurylyk, 2016; Sjöberg et al., 2021) and evaporation (Gao et al., 2021). In this regard, both large-scale
269 and regional modeling indicate that thawing permafrost enhances evapotranspiration (Qin et al., 2017;
270 Wang et al., 2020b). Qin et al. (2017) also report that the increase in evaporation is logically
271 concomitant with a decrease in the runoff coefficient. Additionally, permafrost stores water as ground
272 ice and its thawing can trigger the release of liquid water in the watershed, contributing up to 15% of
273 the annual river streamflow (Cheng and Jin, 2013; Yang et al., 2019).

274 These hydrological changes are tied to various interdependent climate-driven physical processes
275 happening at the ground surface and subsurface (e.g. surface energy balance, infiltration, water phase
276 change, heat conduction...). Because these processes exhibit a strong spatial variability in high mountain
277 environments, it is challenging to represent them accurately together on large spatial scales. Therefore,
278 a deeper understanding of the impact of ground thermo-hydrological changes on the High Asia water
279 cycle can be gained through small-scale physical modeling of these processes. Yet, for now, physics-
280 based approaches at the catchment scale aiming to connect the ground thermo-hydrological regime and
281 the observed hydrological changes on the QTP (such as lake level changes) remain scarce. They are
282 however a powerful approach to tackle the question: how much might climate-driven ground thermal

a supprimé: Seasonal thawing and freezing of the active layer are driven by the surface energy balance and, in return, influences surface and subsurface runoff (Kurylyk et al., 2014; Sjöberg et al., 2021; Walvoord and Kurylyk, 2016) and evaporation (Gao et al., 2021). In this regard, both large-scale and regional modeling indicate that thawing permafrost enhances evapotranspiration (Qin et al., 2017; Wang et al., 2020b). Qin et al. (2017) also report that the increase in evaporation is logically concomitant with a decrease in the runoff coefficient. Additionally, permafrost stores water as ground ice and its thawing can trigger the release of liquid water in the watershed, contributing up to 15% of the annual river streamflow (Cheng and Jin, 2013; Yang et al., 2019).

a supprimé: The aforementioned

297 changes affect the water cycle in high mountain headwater regions? In this study, we use physical land
298 surface modeling to quantify the ground thermo-hydrological changes in an endorheic Tibetan
299 catchment over the last 40 years as a response to climate change. We show the interplay in the water
300 and energy fluxes occurring between the atmosphere, the surface and the subsurface and discuss their
301 impact on the hydrology of the catchment and their implication regarding lake level variations.

a supprimé: might

2. Study area: the Paiku catchment

The Paiku catchment is located in south-western Tibet, China, close to the border with Nepal (28.8°N - 85.6°E, Fig. 1). Its southern edge lies 7 km from the Shishapangma peak (8027 masl). The catchment is endorheic and spans over 78 km from North to South, 66 km from East to West and covers 2 400 km². The median elevation of the catchment is 4872 masl, ranging from 7272 masl to its lowest point, lake Paiku at 4580 masl. Geologically, the catchment is mainly located in the Tethys Himalayan, and thus, an important part of the formations underlying the catchment are metamorphized sedimentary series (Appendix B, Fig. B1). The southern part of the catchment crosses the Southern Tibetan Detachment, and thus, the southern ridges of the massif belong to the High Himalayan metamorphic formations in the west and to the High Himalayan leucogranites of the Shishapangma massif on the east. The north and north-east ridges are formed by granite intrusions surrounded by metamorphic domes. The inner part of the catchment presents Plio-Quaternary formations such as alluvial fans close to the ridges and inclined alluvial plains in its inner parts (Aoya et al., 2005; Searle et al., 1997; Wünnemann et al., 2015).

Automatic Weather Station (AWS) observations (5033 masl, Oct 2019 – Sept 2021, Fig. 1) show that the climate in the catchment is characterized by a relatively small temperature amplitude during the year (around 20 °C, JJA being the warmest months and DJF the coldest) and significant daily amplitude (up to 10 °C during the warm season). The mean annual temperature is -1.5 °C at the AWS, where night freezing can occur until the beginning of June and resume at the beginning of October. The catchment is dry (200-300 mm year⁻¹) and precipitation mostly falls as rain during the monsoon (JJAS).

Around 5% of the catchment is covered by glaciers (RGI Consortium, 2017), which are concentrated in its southwestern part. They feed several proglacial lakes that can reach up to 6 km in length. Geodetic glacier mass budgets show that, similar to other glaciers in the region, glaciers of the Paiku catchment have undergone sustained mass loss at least since the 1970s, with an average mass balance of -0.3 m w.e.a⁻¹ until the beginning of the 2000s and around -0.4 m w.e.a⁻¹ thereafter (Bhattacharya et al., 2021). There are more than 10 rivers that drain the catchment towards the lake and most of them only exhibit a seasonal activity during the monsoon months. The three main ones are

a supprimé: <#>Study area: the Paiku catchment¶

The Paiku catchment is located in south-western Tibet, China, close to the border with Nepal (28.8°N - 85.6°E, Fig. 1). Its southern edge lies 7 km from the Shishapangma peak (8027 masl). The catchment is endorheic and spans over 78 km from North to South, 66 km from East to West and covers 2 400 km². The median elevation of the catchment is 4872 masl, ranging from 7272 masl to its lowest point, lake Paiku at 4580 masl. Geologically, the catchment is mainly located in the Tethys Himalayan, and thus, an important part of the formations underlying the catchment are metamorphized sedimentary series. The southern part of the catchment crosses the Southern Tibetan Detachment, and thus, the southern ridges of the massif belong to the High Himalayan metamorphic formations in the west and to the High Himalayan leucogranites of the Shishapangma massif on the east. The north and north-east ridges are formed by granite intrusions surrounded by metamorphic domes. The inner part of the catchment presents Plio-Quaternary formations such as alluvial fans close to the ridges and inclined alluvial plains in its inner parts (Appendix B, Fig. B0, Aoya et al., 2005; Searle et al., 1997; Wünnemann et al., 2015).¶

a supprimé: Around 5% of the catchment is covered by glaciers (RGI Consortium, 2017), which are concentrated in its southwestern part. They feed several proglacial lakes that can reach up to 6 km in length. Geodetic glacier mass budgets show that, similar to other glaciers in the region, glaciers of the Paiku catchment have undergone sustained mass loss at least since the 1970s, with an average mass balance of -0.3 m w.e.a⁻¹ until the beginning of the 2000s and around -0.4 m w.e.a⁻¹ thereafter (Bhattacharya et al., 2021). There are more than 10 rivers that drain the catchment towards the lake and most of them only exhibit a seasonal activity during the monsoon months. The three main ones are (Fig. 1), Daqu (glacier-fed, 450 km²), Bulaqu (glacier-fed, 325 km²) and Barixiongqu (non-glacier-fed, 703 km²) (Lei et al., 2018).¶

367 (Fig. 1), Daqu (glacier-fed, 450 km²), Bulaqu (glacier-fed, 325 km²) and Barixiongqu (non-glacier-fed,
368 703 km², Lei et al., 2018).

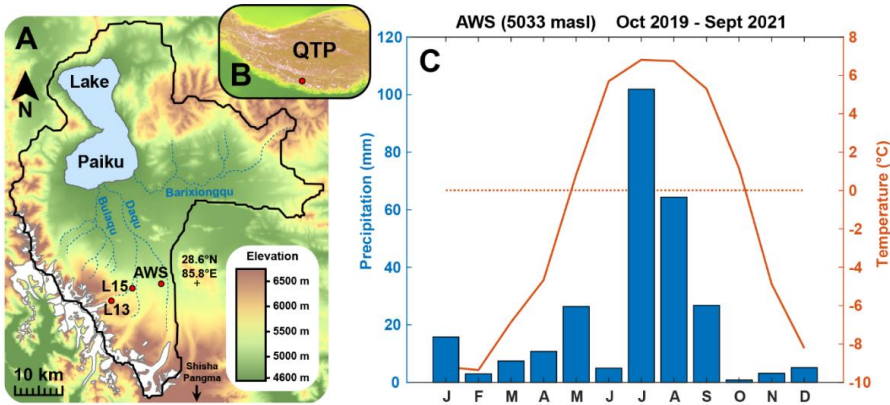
369 In the north-west of the catchment, Lake Paiku covers approx. 280 km² (11.5% of the catchment
370 surface area) and spans over 27 km from North to South. It has a mean water depth of 41 m, with a
371 maximum water depth of 73 m (Lei et al., 2018). It receives water from direct precipitation and from
372 land and glacier runoff which can be routed at the surface via the river systems or the subsurface via
373 the alluvial formations. Because it is hydrologically closed, the lake mainly loses water through
374 evaporation. Previous studies reported lake level fluctuations over different time scales. It reached 4665
375 masl (85 m higher than the present level) prior to 25 ka BP and at the onset of the Holocene (11.9-9.5
376 ka BP), afterwards, the lake shrank gradually (Wünnemann et al., 2015). More recently, the lake level
377 decreased by 3.7 m between 1972 and 2015, losing 4.2% of its surface and 8.5% of its volume,
378 Measurements have been performed since the end of the 1970s and allow to accurately know the
379 evolution of the lake level until today (Lei et al., 2021, 2018), they are used in this study to validate our
380 hydrological results (Sect 3.2.1, Fig. 5D and 6B). At the seasonal scale, the lake level cycle has an
381 amplitude of ~ 0.4 m. It is marked by a strong increase during the monsoon period (JJAS) supported by
382 direct precipitation, glacier melt and land runoff. From October and until the next monsoon period,
383 evaporation dominates the lake mass budget and the level decreases rapidly until January and at a slower
384 rate afterwards (Lei et al., 2021).

a supprimé: north to south. It has a mean water depth of 41 m, with a maximum water depth of 73 m (Lei et al., 2018).

a supprimé:). Afterwards, the lake shrank gradually (Wünnemann et al., 2015).

a supprimé: (Lei et al., 2018).

a supprimé: (Lei et al., 2021).



391
 392 *Figure 1. The Paiku Catchment. A: Topographic and hydrologic map of the catchment with the glaciers*
 393 *in white, the ephemeral rivers in dark blue and the lake in light blue (elevation: SRTM data courtesy of*
 394 *the U.S. Geological Survey). AWS: Automatic Weather Station. L13 and L15 are surface temperature*
 395 *loggers (Sect. 3.1). B: Localization of the catchment over the QTP. C: Monthly temperature and*
 396 *precipitation recorded at the AWS between October 2019 and September 2021.*

397 3. Material and methods

398 3.1. Field measurements

399 An AWS was set up in October 2019 in the South of the catchment at an elevation of 5033 masl
400 (Fig. 1). It is equipped with various sensors which record air temperature, pressure, relative humidity,
401 wind speed, incoming and outgoing long and short wave radiations and precipitation every 15 minutes.
402 The meteorological record extends to September 2021 and covers a period of nearly 2 years. We used
403 it to evaluate and correct the distributed downscaled climatic forcing on which we rely in our modeling
404 framework (Sect. 3.2.2.).

a supprimé: on

405 Two temperature loggers recorded the surface temperature in the vicinity of the AWS location.
406 Logger 15 (L15) is located at 5055 masl, 6 km west of the AWS. Logger 13 (L13) is located at 5356
407 masl, 12 km west of the AWS (Fig. 1). Both loggers were buried 10 to 15 cm below the surface to avoid
408 direct solar radiation on the sensors and recorded surface temperature at a 20-minute timestep from
409 October 2017 to October 2018. These surface temperature records were used to evaluate the simulations
410 (Sect. 3.2.4.).

411 3.2. Catchment thermo-hydrological modeling

412 3.2.1. Conceptual hydrological model for the catchment

413 To understand the level variations of lake Paiku over the last 40 years (1980-2019 period), we
414 develop an approach at the catchment scale. Because the catchment is hydrologically closed, the lake
415 receives water input via direct precipitation, land surface and subsurface runoff, and glacier runoff.
416 Conversely, it loses mass via evaporation. Because the quantification of water flows between the lake
417 and potential aquifers surrounding it is difficult (Rosenberry et al., 2015), our approach assumes that
418 these flows are negligible. The present study requires quantification of the different terms of the
419 hydrological balance. Under these assumptions, the hydrological balance of the lake is given by the
420 following equation:

a mis en forme : Espace Avant : 54 pt

a supprimé: Because the quantification of water flows between the lake and potential aquifers surrounding it is difficult (Rosenberry et al., 2015), our approach assumes that these flows are negligible.

$$\Delta Z_{\text{Lake}} = \text{Precipitation}_{\text{Lake}} + \text{Runoff}_{\text{Land}} + \text{Runoff}_{\text{Glacier}} - \text{Evaporation}_{\text{Lake}}$$

The production of forcing data for the catchment (including precipitation) is detailed in Sect. 3.2.2.

The land hydrology processes are quantified using the CryoGrid community model (version 1.0)

(Westermann et al., 2023) as described in section 3.2.3. Distributed 1D simulations are used to quantify

land evaporation and runoff. The routing of water in the catchment is not represented and the runoff

computed for a given simulation is directly accounted as a water input for the lake. The evaporation

from the lake is simulated using the CryoGrid3-Flake model (Langer et al., 2016) as described in

Section 3.2.5. Glacier melt is not modeled, but estimated for the study period (1980-2019) from remote

sensing observations. From these observations, glacier yield is calculated as described in Sect. 3.2.6.

Our catchment-scale approach to represent the hydrological balance of the lake is summarized in Fig. 2.

Based on this approach, we can evaluate the performance of our framework (Sect. 4.1.2), by comparing

the simulated lake balance with the one derived from the detailed observations of lake level variations

over the study period (Lei et al., 2018, 2021).

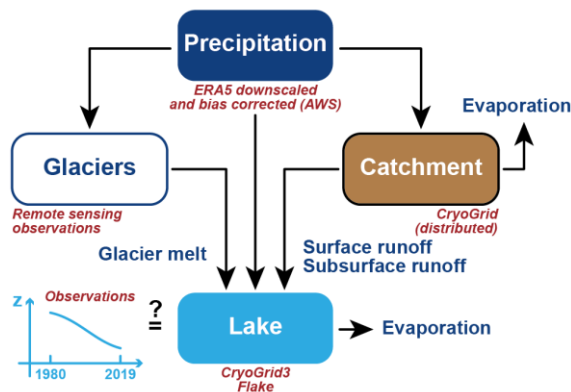


Figure 2. Conceptual hydrological framework for the study.

3.2.2. Forcing data production and validation

In high mountain environments, topography creates strong spatial variability of temperature and

incoming radiation, which impact the surface energy balance (Klok and Oerlemans, 2002) and the

ground thermo-hydrological regime (Magnin et al., 2017). Our approach requires forcing data that (i)

captures this variability, (ii) includes numerous variables such as air temperature, incoming long and

a supprimé: $\Delta Z_{\text{Lake}} = \text{Precipitation}_{\text{Lake}} + \text{Runoff}_{\text{Land}} + \text{Runoff}_{\text{Glacier}} - \text{Evaporation}_{\text{Lake}}$

The production of forcing data for the catchment (including precipitation) is detailed in Sect. 3.2.2. The land hydrology processes are quantified using the CryoGrid community model (version 1.0) (Westermann et al., 2022) as described in section 3.2.3. Distributed 1D simulations are used to quantify land evaporation and runoff. The routing of water in the catchment is not represented and the runoff computed for a given simulation is directly accounted as a water input for the lake. The evaporation from the lake is simulated using the CryoGrid3-Flake model (Langer et al., 2016) as described in Section 3.2.5. Glacier melt is not modeled, but estimated for the study period (1980-2019) from remote sensing observations. From these observations, glacier yield is calculated as described in Sect. 3.2.6. Our catchment-scale approach to represent the hydrological balance of the lake is summarized in Fig. 2.

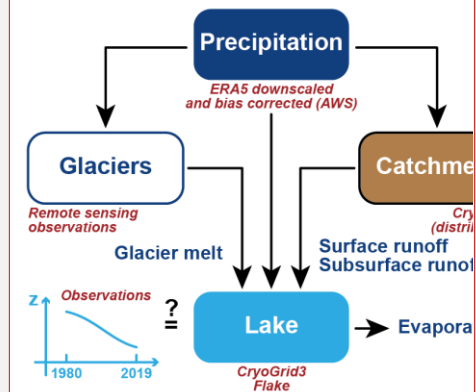


Figure 2. Conceptual hydrological framework for the study.

Forcing data production and validation

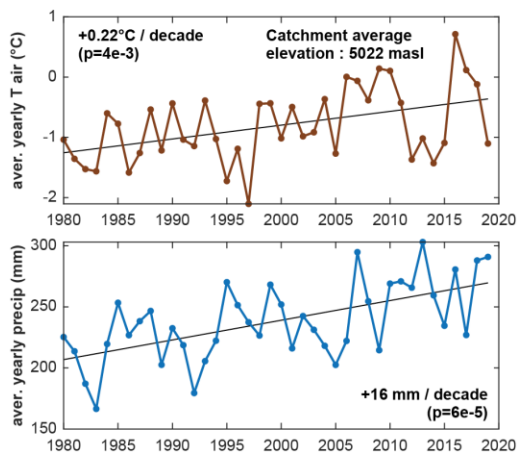
In high mountain environments, topography creates strong spatial variability of temperature and incoming radiation, which impact the surface energy balance (Klok and Oerlemans, 2002) and the ground thermo-hydrological regime (Magnin et al., 2017). Our approach requires forcing data that (i) captures this variability, (ii) includes numerous variables such as air temperature, incoming long and short wave radiations, wind speed, specific humidity, rain and snowfall and (iii) covers the 40 years study period at a sub-daily timestep. The TopoSCALE approach (Fiddes and Gruber, 2014) was developed for this purpose and allows to downscale reanalysis products like ERA5 (Hersbach et al., 2020) at high resolution (here ~ 100 x 100 m). Additionally, because working at a 10⁻² km² spatial resolution over a 2400 km² catchment would require more than 200,000 forcing files and simulations, we rely on the TopoSUB method (Fiddes and Gruber, 2012) to reduce computational costs. This method uses a SRTM30 Digital Elevation Model to explore redundancies in physiographic parameters of the study area such as elevation, aspect, slope and sky-view factor and to identify groups of high-resolution pixels (100 x 100 m) sharing similar values for these parameters. From there, all the high-resolution pixels belonging to such a group are only described as a single TopoSUB point, for which climatic variables can be downscaled to create one single dataset of climatic timeseries. The degree of similarity required by

557 short wave radiations, wind speed, specific humidity, rain and snowfall and (iii) covers the 40 years
558 study period at a sub-daily timestep. The TopoSCALE approach (Fiddes and Gruber, 2014) was
559 developed for this purpose and allows to downscale reanalysis products like ERA5 (Hersbach et al.,
560 2020) at high resolution (here ~ 100 x 100 m).

561 Additionally, because working at a 10^{-2} km² spatial resolution over a 2400 km² catchment would
562 require more than 200.000 forcing files and simulations, we rely on the TopoSUB method (Fiddes and
563 Gruber, 2012) to reduce computational costs. This method uses a SRTM30 Digital Elevation Model to
564 explore redundancies in physiographic parameters of the study area such as elevation, aspect, slope and
565 sky-view factor and to identify groups of high-resolution pixels (100 x 100 m) sharing similar values
566 for these parameters. From there, all the high-resolution pixels belonging to such a group are only
567 described as a single TopoSUB point, for which climatic variables can be downscaled to create one
568 single dataset of climatic timeseries. The degree of similarity required by TopoSUB to identify groups
569 of high-resolution pixels with redundant physiographic parameters can be adjusted by choosing the final
570 number of TopoSUB points (and thus climate datasets) that should be used to cover the area
571 corresponding to one ERA5 pixel. The Paiku catchment intersects 8 ERA5 pixels at 30 km resolution
572 and we chose to use 50 TopoSUB points within each ERA5 pixel to cover the spatial variability created
573 by the topography on small-scale climate. Ultimately, 368 TopoSUB points are used to cover the
574 catchment. The average level of redundancy (i.e. the average number of high-resolution pixels
575 represented by a single TopoSUB point) is 723 ± 745 (1σ , median: 506, min: 1, max: 4347). Appendix
576 C, Fig. C1 shows the distribution of the TopoSUB points and a reconstruction of the topography of the
577 catchment based on this approach. The period covered by the forcing datasets starts on 1st January 1980
578 and ends on 31st August 2020 (40 years and 8 months).

579 In the TopoSCALE statistical downscaling approach, we do not rely on the AWS data and thus the
580 downscaled ERA5 data can be biased, as is often the case over Asia (Jiang et al., 2021, 2020; Jiao et
581 al., 2021; Orsolini et al., 2019). Comparison against the available AWS observations (Appendix D, Fig.
582 D1) indeed highlights notable differences in variables such as air temperature and precipitation. From
583 these differences, we derived monthly bias correction factors that we applied systematically to all of the
584 368 climate forcing datasets. The catchment averages for precipitation and air temperatures are shown

585 in Fig. 3. In this figure and across the rest of the study, we use p-values to evaluate the significance of
 586 linear trends in the temporal evolution of certain variables (temperature, precipitation, evaporation...).
 587 This p-value tests the null hypothesis which supposes that the value of the slope is equal to zero. The
 588 hypothesis is tested using the Student's t-test, by comparing the distance between the estimated slope
 589 and 0, relative to the standard error of the slope. We did not report trends when this p-value (probability
 590 of a null slope) was higher than 0.005.



591 *Figure 3. Climate forcing data for the land and lake modeling. Annual catchment-average air*
 592 *temperature (2 m above ground) and annual total precipitation for the study period. Note that the model*
 593 *is also forced by incoming short and long wave radiations, humidity, windspeed and air pressure.*
 594 *Details about the spatial and temporal resolution of the distributed forcing data are presented in Sect.*
 595 *3.2.2.*
 596
 597
 598

3.2.3. The CryoGrid community model (version 1.0)

599 To simulate the ground thermo-hydrological regime, we use the CryoGrid community model
 600 (Westermann et al., 2023). The CryoGrid community model (CG) is a land surface model designed for
 601 applications in cold regions where seasonal frozen ground or permafrost may occur. The model
 602 implements heat transfer in a 1D soil column, accounting for freeze-thaw processes of soil water using
 603 effective heat capacity (Nakano and Brown, 1972). To do so, soil freezing curves are based on
 604 Dall'Amico et al. (2011) as detailed in (Westermann et al., 2013). Vertical water movement in the soil
 605 column is based on Richards equation (Richardson, 1922; Richards, 1931). The soil matric potential
 606 and hydraulic conductivity follow van Genuchten, (1980) and Mualem (1976). Additionally, to
 607 represent the obstruction of connected porosity by ice formation, the hydraulic conductivity is reduced

a supprimé: To simulate the ground thermo-hydrological regime, we use the CryoGrid community model (Westermann et al., 2022). The CryoGrid community model (CG) is a land surface model designed for applications in cold regions where seasonal frozen ground or permafrost may occur. The model implements heat transfer in a 1D soil column, accounting for freeze-thaw processes of soil water using effective heat capacity (Nakano and Brown, 1972). To do so, soil freezing curves are based on Dall'Amico et al. (2011) as detailed in Westermann et al. (2013). Vertical water movement in the soil column is based on Richards equation (Richards, 1931; Richardson, 1922). The soil matric potential and hydraulic conductivity follow van Genuchten (1980) and Mualem (1976). Additionally, to represent the obstruction of connected porosity by ice formation, the hydraulic conductivity is reduced by a factor dependent on the local ice content, following Dall'Amico et al. (2011). The model features the snowpack module called *CG Crocus* described in Zweigel et al. (2021) that adapts the snow physics parameterizations from the CROCUS scheme (Vionnet et al., 2012) to the native snow module of CryoGrid3 (Westermann et al., 2016). At the surface, the model uses a surface energy balance module to calculate the ground surface temperature and water content. The turbulent fluxes of sensible and latent heat are calculated using a Monin-Obukhov approach (Monin and Obukhov, 1954). Evaporation is derived from the latent heat fluxes using the latent heat of evaporation and is adjusted to the available water in the soil. It occurs in the first grid cell only, but water can be drawn upwards due to matric potential differences. Because vegetation is very scarce in the catchment, we do not expect transpiration to have a strong imprint on evapotranspiration and our calculations do not unravel evaporation from transpiration.¶

Model setup and validation¶

The setup of the CryoGrid community model for the land is presented in Fig. 4. To capture the high spatial variability of mountainous climate, our approach relies on the 368 climate forcing datasets to cover the catchment (see section 3.2.2). This approach enables us to perform spatially distributed modeling. All of the 368 simulations are independent and use the same parameterization. In absence of direct observation of the soil stratigraphy within the catchment, the soil column was designed to agree with field observations in the region (Hu et al., 2020; Luo et al., 2020; Wang et al., 2008, 2009; Yang et al., 2014b; Yuan et al., 2020), to be consistent with similar modeling approaches across Tibet (Chen et al., 2018; Song et al., 2020) and to be consistent with input datasets (Shangguan et al., 2013, 2017). Thus, the soil stratigraphy is divided into 3 units: a top soil (0.3 m thick), a bottom soil (1.7 m thick), and a bedrock unit (extending beyond the depth of interest of the study). An overview of the parameters for each unit, their source and the way they are calculated is presented in Appendix A, Tab. A1. Regarding the processes implemented in the model (Sect. 3.2.3), infiltration according to Richards equation only occurs in the top and bottom soil units. The bedrock unit has a static water content. Unraveling surface from subsurface flow is an ongoing challenge in catchment-scale hydrology (McDonnell, 2013) and this distinction is important in mountain terrains where these two flows can behave differently due to the complex topography (Gao et al., 2014; Seibert et al., 2003). For this study, we rely on a simple approach that computes surface and subsurface flow as follows.¶

671 by a factor dependent on the local ice content, following Dall’Amico et al. (2011). The model features
672 the snowpack module called CG Crocus described in Zweigel et al. (2021) that adapts the snow physics
673 parameterizations from the CROCUS scheme (Vionnet et al., 2012) to the native snow module of
674 CryoGrid3 (Westermann et al., 2016). At the surface, the model uses a surface energy balance module
675 to calculate the ground surface temperature and water content. The turbulent fluxes of sensible and
676 latent heat are calculated using a Monin–Obukhov approach (Monin and Obukhov, 1954). Evaporation
677 is derived from the latent heat fluxes using the latent heat of evaporation and is adjusted to the available
678 water in the soil. It occurs in the first grid cell only, but water can be drawn upwards due to matrix
679 potential differences. Because vegetation is very scarce in the catchment, we do not expect transpiration
680 to have a strong imprint on evapotranspiration and our calculations do not unravel evaporation from
681 transpiration.

682 3.2.4. Model setup and validation

683 The setup of the CryoGrid community model for the land is presented in Fig. 4. To capture the
684 high spatial variability of mountainous climate, our approach relies on the 368 climate forcing datasets
685 to cover the catchment (see section 3.2.2). This approach enables us to perform spatially distributed
686 modeling. All of the 368 simulations are independent and use the same parameterization. In absence of
687 direct observation of the soil stratigraphy within the catchment, the soil column was designed to agree
688 with field observations in the region (Yuan et al., 2020; Wang et al., 2009; Hu et al., 2020; Luo et al.,
689 2020; Yang et al., 2014b; Wang et al., 2008), to be consistent with similar modeling approaches across
690 Tibet (Chen et al., 2018; Song et al., 2020) and to be consistent with input datasets (Shangguan et al.,
691 2013, 2017). Thus, the soil stratigraphy is divided into 3 units: a top soil (0.3 m thick), a bottom soil
692 (1.7 m thick), and a bedrock unit (extending beyond the depth of interest of the study). An overview of
693 the parameters for each unit, their source and the way they are calculated is presented in Appendix A,
694 Tab. A1.

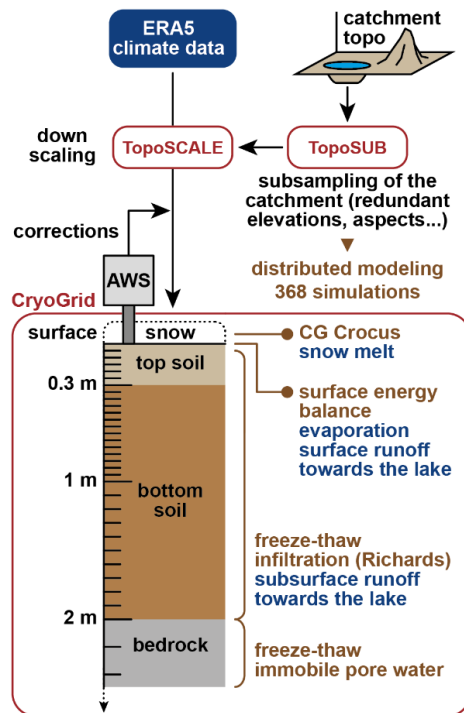
695 Regarding the processes implemented in the model (Sect. 3.2.3), infiltration according to Richards
696 equation only occurs in the top and bottom soil units. The bedrock unit has a static water content.
697 Unraveling surface from subsurface flow is an ongoing challenge in catchment-scale hydrology
698 (McDonnell, 2013) and this distinction is important in mountain terrains where these two flows can

699 behave differently due to the complex topography (Seibert et al., 2003; Gao et al., 2014; Hu et al.,
700 2020). For this study, we rely on a simple approach that is based on thresholds regarding the soil water
701 content (porosity and field capacity). This kind of approaches are thus based on soil properties and have
702 often been used in hydrological modeling studies (Vörösmarty et al., 1989; Shaman et al., 2002;
703 Kelleners et al., 2010; Kampf, 2011; Samuel et al., 2008). In detail, we compute surface and subsurface
704 flow as follows.

705 On the one hand, surface runoff is computed relative to the saturation level of the soil column.
706 When the entire soil column is saturated ($WC = \text{porosity}$), additional water input from precipitation or
707 snowmelt is directly counted as surface runoff. On the other hand, subsurface runoff is computed
708 relative to the field capacity of the ground, which is an input parameter of the model. When the water
709 content (WC) of a ground cell exceeds this field capacity (FC), the amount of water corresponding to
710 $WC - FC$ is available to produce subsurface runoff. We use the lateral boundary condition
711 `LAT_WATER_RESERVOIR` from the CryoGrid community model (Westermann et al., 2023) to
712 account for this subsurface runoff. The speed at which this available water exits the soil column towards
713 the lake is calculated with Darcy's law, using the hydrological conductivity of the ground and the mean
714 slope of the catchment as hydraulic slope.

715 Because we do not have knowledge of the distributed thermal state with depth over the catchment
716 at the beginning of the simulations, we assume temperature profiles were in equilibrium with the climate
717 of the 5 first years of modeling (1980-1984). To do so, we start our simulations with a 60-year spin-up
718 of these first 5 years (12 repetitions), which is sufficient to establish a stable temperature profile over
719 the first 9 to 80 meters depending on the simulations, extending beyond the hydrologically active part
720 of the ground (the first 2 meters).

a supprimé: 2022



722 Figure 4. Modeling framework for the land hydrology. ERA5 data are downscaled using the TopoSUB
 723 and TopoSCALE approaches (Fiddes and Gruber, 2014, 2012). The downscaled data are bias-
 724 corrected based on the AWS observations. Distributed 1D simulations are performed using the
 725 CryoGrid community model (Westermann et al., 2023). The vertical resolution is indicated with the tick
 726 marks on the depth axis.

a supprimé: ERA5 data are downscaled using the TopoSUB and TopoSCALE approaches (Fiddes and Gruber, 2012, 2014). The downscaled data are bias-corrected based on the AWS observations. Distributed 1D simulations are performed using the CryoGrid community model (Westermann et al., 2022).

727
 728
 729 To validate model simulations, the simulated ground surface temperatures (GST) are compared to
 730 the two temperature logger time series acquired in the vicinity of the AWS (Sect. 3.1). We used this
 731 comparison to calibrate the surface roughness used for the surface energy balance calculations in the
 732 model.

733 The following method is used to produce area-averaged evaporation and runoff (in mm water
 734 equivalent) in a zone of interest. For a given TopoSUB point in this zone, the model produces
 735 hydrological values in m^3 using the area of a TopoSUB pixel on the catchment map. Then these values
 736 are multiplied by the number of pixels in the zone corresponding to this TopoSUB point in particular,
 737 and this for all the relevant TopoSUB points covering the zone (e.g. evaporation in warm permafrost).
 738 Then the area of interest is calculated by counting the number of pixels in the zone of interest and

745 multiplying this number by the area of a pixel. Then the total volume is divided by the total surface for
746 the zone of interest to obtain the final value in mm.

747 3.2.5. Lake modeling

748 The lake thermo-hydrological response to the climatic forcing data is simulated using the
749 CryoGrid3-Flake model (Langer et al., 2016). The two models were coupled by Langer et al. (2016) to
750 simulate the thermal regime of thermokarst lakes (including surficial water freezing and melting) and
751 underlying ground. Here we use the coupled models mainly to quantify evaporation at the lake surface.
752 In the coupled model, the native surface energy balance module of CryoGrid3 (Westermann et al., 2016)
753 was amended to account for processes tied to free water surface energy balance: (i) the dependence of
754 the albedo of a water surface to solar angle (and thus time of the day) and wind speed (and wave
755 formation), (ii) the dependence of the surface roughness length to wind speed (and wave formation) and
756 (iii) the exponential decay of incoming radiation with depth in the water column. Similar to the land
757 simulations, the lake simulations were forced by the downscaled ERA5 data (with the TopoSUB and
758 TopoSCALE methodology), with the corrections derived from the AWS data (Sect. 3.2.2). The
759 simulations were initiated with a 20-year spin-up of the 1980-1984 climate. The simulation results
760 corresponding to the four ERA5 tiles covering the lake were then averaged using the respective spatial
761 footprint of each tile on the lake.

762 3.2.6. Quantification of glacier mass change

763 Multiple studies quantified the volume change of the glaciers located within the Paiku catchment
764 in the recent past (1970s to 2020). To our knowledge, there are no field based measurements of glacier
765 mass balance available in this catchment. As a consequence, we rely solely on geodetic mass balance
766 studies (Brun et al., 2017; Maurer et al., 2019; King et al., 2019; Shean et al., 2020; Hugonnet et al.,
767 2021). All these studies estimated glacier volume changes over periods of 20-30 years from satellite
768 derived DEMs. As a consequence, we can only estimate the average annual glacier mass balance, and
769 not the year-to-year variability. Glaciers occupy approximately 113 km² in the Paiku catchment. They
770 have shrunk for the past fifty years at a rate of 0.44 % y⁻¹, from an area of 132 km² in 1975 to 122 km²
771 around 2000 and to their current extent (King et al., 2019; Bolch et al., 2019). The average mass
772 balances for the period 1975-2000 and 2000-2020 are $-3.9 \pm 2.1 \times 10^{10}$ kg y⁻¹ and $-5.4 \pm 2.4 \times 10^{10}$ kg y⁻¹,

a supprimé: The lake thermo-hydrological response to the climatic forcing data is simulated using the CryoGrid3-Flake model (Langer et al., 2016). The two models were coupled by Langer et al. (2016) to simulate the thermal regime of thermokarst lakes (including surficial water freezing and melting) and underlying ground. Here we use the coupled models mainly to quantify evaporation at the lake surface. In the coupled model, the native surface energy balance module of CryoGrid3 (Westermann et al., 2016) was amended to account for processes tied to free water surface energy balance: (i) the dependence of the albedo of a water surface to solar angle (and thus time of the day) and wind speed (and wave formation), (ii) the dependence of the surface roughness length to wind speed (and wave formation) and (iii) the exponential decay of incoming radiation with depth in the water column. Similar to the land simulations, the lake simulations were forced by the downscaled ERA5 data (with the TopoSUB and TopoSCALE methodology), with the corrections derived from the AWS data (Sect. 3.2.2). The simulations were initiated with a 20-year spin-up of the 1980-1984 climate. The simulation results corresponding to the four ERA5 tiles covering the lake were then averaged using the respective spatial footprint of each tile on the lake.

-----Saut de page-----

¶ Quantification of glacier mass change ¶

Multiple studies quantified the volume change of the glaciers located within the Paiku catchment in the recent past (1970s to 2020). There are no field based measurements of glacier mass balance available in this catchment to our knowledge. As a consequence, we rely solely on geodetic mass balance studies (Brun et al., 2017; Hugonnet et al., 2021; King et al., 2019; Maurer et al., 2019; Shean et al., 2020). All these studies estimated glacier volume changes over periods of 20-30 years from satellite derived DEMs. As a consequence, we can only estimate the average annual glacier mass balance, and not the year to year variability. Glaciers occupy approximately 113 km² in the Paiku catchment. They have shrunk for the past fifty years at a rate of 0.44 % y⁻¹, from an area of 132 km² in 1975 to 122 km² around 2000 and to their current extent (Bolch et al., 2019; King et al., 2019). The average mass balances for the period 1975-2000 and 2000-2020 are $-3.9 \pm 2.1 \times 10^{10}$ kg y⁻¹ and $-5.4 \pm 2.4 \times 10^{10}$ kg y⁻¹, respectively ($-4.6 \pm 2.5 \times 10^7$ m³ and $-6.4 \pm 2.8 \times 10^7$ m³ with a 850 kg m⁻³ density). These mass balances correspond to specific mass balances of -0.31 ± 0.17 m of water equivalent per year (w.e. y⁻¹) and -0.47 ± 0.21 m w.e. y⁻¹, respectively.

-----Saut de page-----

¶ Results ¶

823 respectively ($-4.6 \pm 2.5 \cdot 10^7 \text{ m}^3$ and $-6.4 \pm 2.8 \cdot 10^7 \text{ m}^3$ with a 850 kg m^{-3} density). These mass balances
824 correspond to specific mass balances of $-0.31 \pm 0.17 \text{ m}$ of water equivalent per year (w.e. yr^{-1}) and -0.47
825 $\pm 0.21 \text{ m w.e. yr}^{-1}$, respectively.

826 Regarding glacial runoff, it was estimated to $320 \pm 4 \text{ mm}$ per year for the 2001-2010 period by
827 Biskop et al. (2016) using a temperature-index approach for ice melt. For the 2000-2018 period, Zhang
828 et al. (2020b) derived a runoff value of $52 \pm 12 \text{ mm}$ per year ($1.24 \pm 0.29 \cdot 10^8 \text{ m}^3$ per year that we scaled
829 to the basin area). The value we derive of $39 \pm 13 \text{ mm}$ per year thus finds good consistency with the
830 latter one (Sect. 4.1).

4. Results

4.1. Model validation and hydrological budget of Lake Paiku

4.1.1. Model validation

Simulated daily ground surface temperatures are in good agreement with the observed ones, showing a bias of $-0.2\text{ }^{\circ}\text{C}$ and $0.6\text{ }^{\circ}\text{C}$ and a RMSE of $1.4\text{ }^{\circ}\text{C}$ and $1.6\text{ }^{\circ}\text{C}$ for loggers 15 and 13, respectively (Fig. 5A and 5C). Most of this RMSE is explained by a mismatch between model and observations in the tails of the temperature distribution, whereas intermediate temperatures exhibit the best agreement with observations.

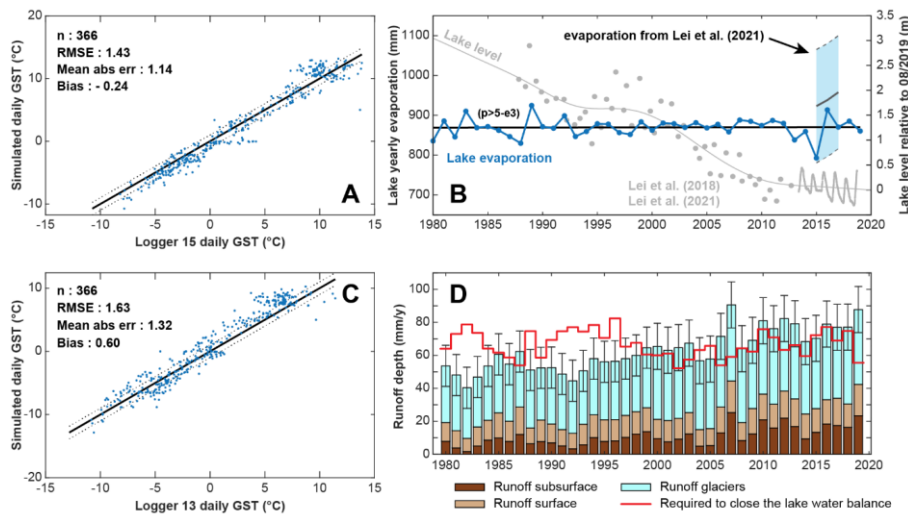


Figure 5. Model validation. A and C: modeled mean daily ground surface temperatures compared to measured ground surface temperatures for logger 15 and logger 13 (location on Fig. 1). B: modeled annual lake evaporation (blue curve) and comparison with values calculated by Lei et al. (2021) in the light blue zone. The gray curve shows the smoothed lake level relative to August 2019 based on observations from Lei et al. (2018) (gray points) and Lei et al. (2021) (gray oscillating line). D: Comparison between the runoffs required to reproduce the observed lake variations (red curve, derived from lake level, lake area, forcing data and lake evaporation) and the sum of the glacier and land runoff we derive from remote sensing observations and modeling respectively (Sect. 3.2). Error bars are associated to the glacier values and come from the geodetic results. Runoff values are expressed as heights scaled to the land surface of the Paiku catchment.

Annual lake evaporation mainly ranges between 800 and 900 mm per year (Fig. 5B), with a mean value of $870 \pm 23\text{ mm}$ (1σ). Lake evaporation does not exhibit a linear trend of increase or decrease and is mostly dominated by year-to-year variability. Though slightly lower, our evaporation results are in

a mis en forme : Police :12 pt, Italique

a mis en forme : Police :12 pt, Italique

a mis en forme

a supprimé: and lake evaporation

a supprimé: Though slightly lower, our evaporation results are in agreement with the values from Lei et al. (2021),

857 good agreement with the values from Lei et al. (2021), which are derived from local and regional
858 meteorological observation and lake budget calculation (Fig. 5B). We used the simulated evaporation
859 together with the lake level data and lake area data from Lei et al. (2018) and Lei et al. (2021) and the
860 precipitation forcing datasets (3.2.2) to derive the total runoff (land + glacier) required as an input to
861 the lake budget to reproduce the lake variations. This required runoff corresponds to the red line of
862 Fig. 5D. The required runoff volumes are scaled to the land area of the catchment to be comparable
863 with the other variables. Fig. 5D also presents the runoff values derived from the land cryo-hydrological
864 modeling and from the glacier remote sensing investigations. Annual volumes are expressed as mm
865 over the land part of the catchment (excluding the lake). As presented in section 3.2.6, glacier mass
866 balance values are considered constant for the 1980-2000 period and the 2000-2019 period and are
867 respectively equal to $-4.6 \pm 2.5 \cdot 10^7$ and $-6.4 \pm 2.8 \cdot 10^7$ m³ per year. The addition of annual precipitation
868 to these values to quantify the total glacier runoff introduces year-to-year variability to the glacier
869 runoff. At the catchment scale, the average glacier runoff over the 40 years is 39 ± 13 mm per year.

870 Over the 40 years, the average annual land runoff value (surface + subsurface) we model is 24 ± 8
871 mm. Summed together, the land and glacier runoff find a partial agreement with the runoff that is
872 required to close the lake water balance. Annual values are compatible within error bars for 28 out of
873 the 40 years of simulations. The glacier and land runoff are slightly too small to close the lake water
874 balance during the first 20 years and slightly too large for the last 20 years of simulation. Over the whole
875 period, the sum of the glaciers + land runoff produces 95% of the required runoff. Land runoff is further
876 described in Sect. 4.3 and lake results in section 4.4.

877 4.1.2. Hydrological budget of Lake Paiku

878 Our observations, climate data, simulations, geodetic data and the lake level data from Lei et al.
879 (2018, 2021) enable us to quantify the different terms of the lake hydrological budget. We present these
880 results in m of lake level change based on the average slope of the Volume = f(level) relationship
881 (Fig. 6). As the unique output term, evaporation dominates the lake budget with an average annual value
882 of 0.86 m (34.6 m per 40 years, Fig. 6A). Direct precipitation in the lake is the dominant input with an
883 average annual value of 0.31 m (12.3 m per 40 years), followed by glacier runoff (0.28 m per year, 11.3

a supprimé: We used the simulated evaporation together with the lake level data and lake area data from Lei et al. (2018) and Lei et al. (2021) and the precipitation forcing datasets (3.2.2) to derive the total runoff (land + glacier) required as an input to the lake budget to reproduce the lake variations....

a supprimé:

a déplacé (et inséré) [1]

m per 40 years) and land runoff (0.18 m per year, 7.0 m per 40 years). When compared with lake volume observations over the 40 years of the simulation, the simulated lake budget is 1.04 m too negative.

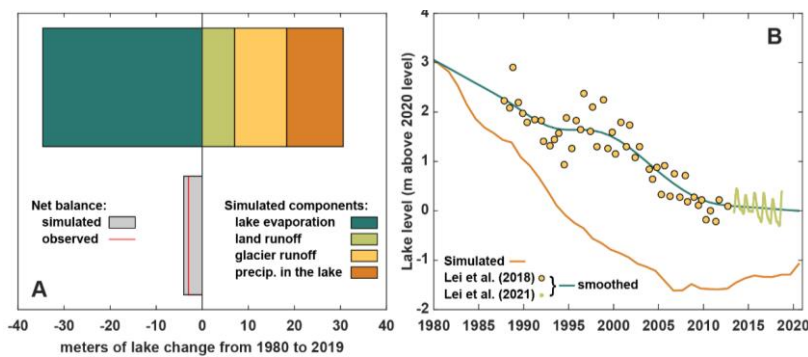


Figure 6. Budget and level of lake Paiku for the simulation period (1980-2019). A. The different components of the hydrological budget of the lake according to our framework. Results are given in m of lake change based on the average slope of the Volume = f(level) relationship. B. Lake level data. Points correspond to observations from Lei et al. (2018, 2021) that we smoothed (green curve, based also on observation points older than 1980). The simulated lake level appears in orange.

Based on our results, we also reconstructed lake level variations that we compare with the observed variations (Fig. 6B). Following our framework, our values are presented at an annual timestep. They qualitatively reproduce the overall lake level decrease but tend to overestimate this decrease and show an increasing mismatch with the observations from 0 in 1980 to 2 meters in 2005. This mismatch is later compensated by an increasing lake level trend in our simulation from 2005 to 2019. At the end of the simulation period, the mismatch is 1.04 m, consistent with the budget values (Fig. 6A) and the fact that our approach provides 95% of the required runoff to close the lake budget (Sect. 4.1.1.). This pattern of a too strong decrease followed by an increase is consistent with the comparison between simulated and required runoff presented on Fig. 5D.

4.2. Ground thermal results

Based on our temperature results, we define four categories of ground thermal regimes (Fig. 7A). Cold permafrost are the areas of the catchment for which the deepest thaw depth did not exceed 1 m over the 40 years of simulation. For cold permafrost, frozen conditions dominate the first meters of the ground most of the year and surficial thawing during summer can be interrupted by ground freezing

a déplacé (et inséré) [2]

a déplacé (et inséré) [3]

a déplacé (et inséré) [4]

a déplacé (et inséré) [5]

a supprimé: 6A

915 from the surface to the top of the permafrost at night. *Warm permafrost* are the areas of the catchment
 916 presenting permafrost for the whole duration of the simulation and which are not part of the *cold*
 917 *permafrost*. These areas are characterized by a distinct seasonal pattern of frozen ground in winter and
 918 an active layer in summer. *Disappearing permafrost* are the areas of the catchment presenting
 919 permafrost at the beginning of the simulation and not at the end. *No permafrost* are the areas without
 920 permafrost at the onset of the simulation. The geographical characteristics of each ground category are
 921 presented in Tab. 1, and their distribution throughout the catchment is shown on Fig. 7A. These different
 922 ground categories are subsequently used to compare their cryo-hydrological behaviors during the
 923 simulation (consistent color code).

924 Table 1. Cryological classification of the catchment based on the modeled ground temperatures.

Name	Characteristics	% of the catchment area	Elevation mean (masl)	Elevation range (masl)	Slope mean (°)
Cold permafrost	Max thaw depth over the 40 years < 1m	3%	6068	6946 5213	35±13
Warm Permafrost	Max thaw depth > 1 m and permafrost present over the 40 years	19%	5480	5921 4877	20±9
Disappearing permafrost	Permafrost present in 1980 but disappears during the simulation	5%	5274	5552 4882	18±9
No permafrost	No permafrost from 1980 to 2019	73%	4900	5463 4580	10±8

925 At the catchment scale, the 2 m depth temperature (Fig. 7B) shows a pronounced warming trend
 926 of 0.17 °C per decade ($p=1\times 10^{-6}$). This trend is mainly supported by the *no permafrost* areas, which
 927 underwent a slightly stronger warming trend of 0.2 °C per decade ($p=7\times 10^{-8}$). Areas with disappearing
 928 permafrost, warm permafrost and cold permafrost exhibit smaller trends around 0.1 °C per decade with
 929 decreasing p-values (respectively 0.00001, 0.006 and 0.05, i.e. non-significant for the last two).

930 From 1980 to 1989, permafrost covers 27% of the catchment and the mean active layer thickness
 931 (ALT) is 1.36 ± 0.51 m (1σ , minimum: 0.11 m and maximum: 2.37 m, Fig. 7C). From 2010 to 2019,
 932 permafrost covers 22% of the catchment. At the scale of the initial permafrost area, this change
 933 corresponds to a loss of 19%. The mean ALT is 1.29 ± 0.49 m (1σ , minimum: 0.11 m and maximum:
 934 2.55 m, Fig. 7D) for this period. Permafrost disappearance (grey zones in Fig. 7D) mainly happens for

a supprimé: 6A

a mis en forme : Police : +Corps(Calibri)

a mis en forme : Police : +Corps(Calibri)

a mis en forme : Police : +Corps(Calibri), Gras

a mis en forme : Police : +Corps(Calibri)

a mis en forme : Police : +Corps(Calibri)

a mis en forme : Police : +Corps(Calibri)

a supprimé: 6B

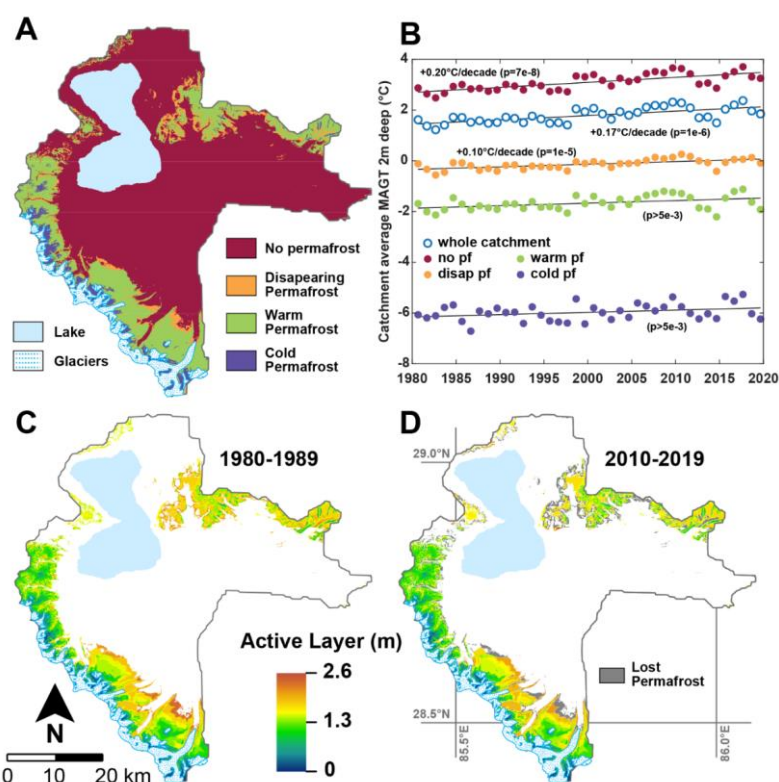
a supprimé: 6C

a supprimé: active layer thickness

a supprimé: 6D

a supprimé: 6D

941 low-lying permafrost of the south and the center of the catchment. It occurs for the most part on the
 942 outer slopes of the permafrost regions and at the bottom of steep glacial valleys.



943 Figure 7. A: Different cryological states of the ground throughout the catchment for the 1980-2019
 944 period (see Tab. 1). B: Annual 2 m deep ground temperature averaged for the whole catchment and for
 946 the different cryological states of the ground. C: Average active layer depth over the 1980-1989 period.
 947 D: Average active layer depth over the 2010-2019 period. Only locations presenting permafrost at the
 948 end of the simulation are assigned a color on the map on C and D. Locations where permafrost has
 949 disappeared are shown in gray on D.

950
 951 We also present the average duration of seasonal thaw at a depth of 70 cm averaged over the
 952 catchment (Fig. 8A). Because at this depth some areas might present two (or more) consecutive years
 953 without thawing (highest locations) or without freezing (lowest locations), these areas were excluded
 954 from the averaging. In the end, the averaged results account for 89% of the catchment land area (i.e.
 955 excluding glaciers and lake Paiku). The results show an increasing trend in the duration of the seasonal
 956 thaw of +4.6 days per decade ($p=3 \times 10^{-4}$, blue line on Fig. 8A). When looking at the average start and
 957 stop days of the seasonal thaw (Fig. 8A, grey lines) in the Julian calendar (day 150 is the 30th of May

a supprimé: 6

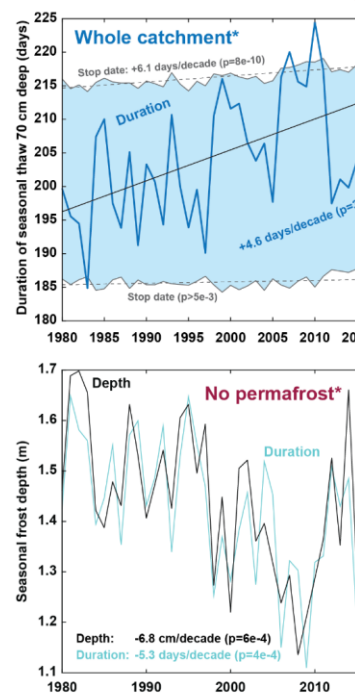
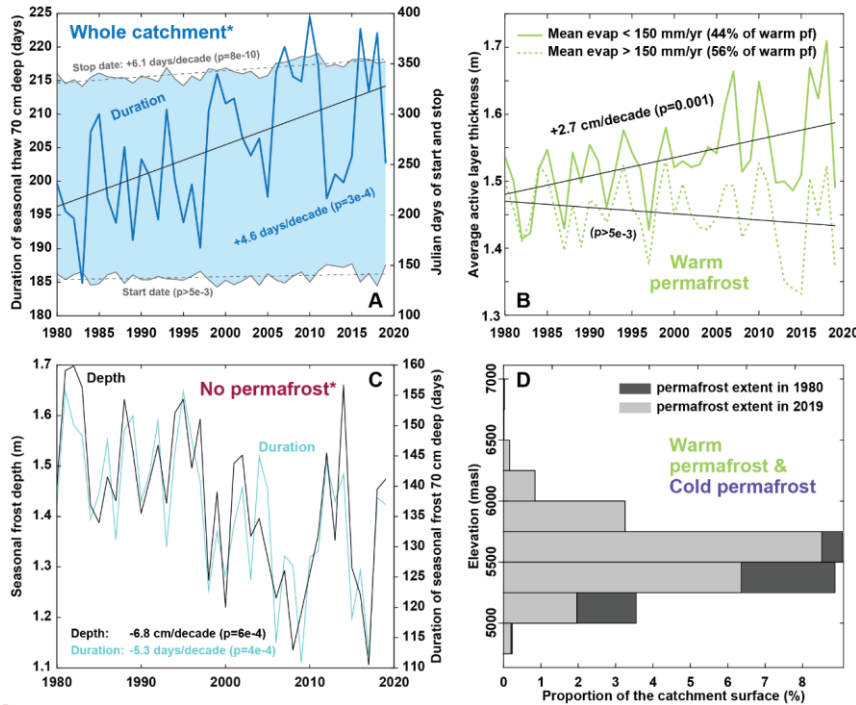
a supprimé: 7A

a supprimé: 7A

a supprimé: 7A

962 and day 300 is the 27th of October), we note that this increase is mainly caused by a later ending date of
 963 the thaw season (*Stop date* on Fig. 8A, +6.1 days per decade, $p=8\times 10^{-10}$) and not by an earlier starting
 964 date (non-significant trend).

a supprimé: 7A



a supprimé:

a supprimé: 7

965
 966 *Figure 8. A: Duration of seasonal thaw 70 cm deep averaged over the catchment. The asterisk indicates*
 967 *that the presented curves average 89% of the surface of the catchment (Sect. 4.2). The gray curves and*
 968 *the light blue area are associated with the right axis and indicate the average start and stop day of the*
 969 *seasonal thaw in the Julian calendar. Values higher than 365 indicate that freezing conditions came*
 970 *back after the 31st of December. B: Active Layer Thickness (ALT) evolution for warm permafrost. The*
 971 *solid line shows the ALT for simulations experiencing an annual evaporation lower than 150 mm when*
 972 *averaged over the 40 years. The dashed line shows the ALT for simulations with annual evaporation*
 973 *higher than 150 mm. C: Temporal trends for seasonally frozen ground where there is no permafrost.*
 974 *The asterisk indicates that simulations were excluded if one of the simulated years did not present*
 975 *freezing conditions 70 cm deep (persistence of thawed conditions from one year to another). The*
 976 *presented curves thus average 88% of the total permafrost-free areas of the catchment. D: Altitudinal*
 977 *distribution of permafrost in 1980 and 2019. This distribution includes both cold and warm permafrost.*
 978

979 Within warm permafrost, we distinguished ALT for locations experiencing an average evaporation
 980 lower or higher than 150 mm per year during the simulations (Fig. 8B). Whereas locations with average
 981 evaporation below 150 mm per year record an active layer deepening trend of 2.7 cm per decade

a supprimé: AL thickness

a supprimé: 7B

987 ($p=0.001$), it is not the case for locations with an average evaporation higher than 150 mm per year
988 (non-significative trend).

989 In the permafrost-free areas of the catchment, seasonal frozen ground (Fig. 8C) reaches a depth of
990 1.43 ± 0.15 m on average and shows a decreasing trend of -6.8 cm per decade ($p=6 \times 10^{-4}$). At a 70 cm
991 depth, the average duration of seasonally frozen ground is 136 ± 12 days with a decreasing trend of -
992 5.3 days per decade ($p=4 \times 10^{-4}$). These values average 88% of the no permafrost areas since locations
993 showing persistent thawed conditions at this depth from one year to another were excluded (i.e. minimal
994 seasonal freezing depth over the 40 years lower than 70 cm).

995 When comparing permafrost spatial distribution between 1980 and 2019 (Fig. 8D), our results
996 show that permafrost distribution above 5750 masl has not been modified during the simulation.
997 Permafrost disappearance has mainly occurred between 5000 and 5750 masl, with the largest loss
998 reaching 2.5% of the catchment area between 5250 and 5500 masl.

999 4.3. Hydrological results for the land

1000 The mean annual evaporation (land area only) over the simulation time is 180 ± 19 mm (1σ , Fig.
1001 9A). Evaporation shows an increasing trend over the 40 years of $+1.01$ mm per decade ($p=3 \times 10^{-7}$).
1002 Average total runoff over the 40 years is 24 ± 8 mm per year (Fig. 9B) and exhibits an increasing trend
1003 of $+4.8$ mm per decade ($p=8 \times 10^{-7}$). Similarly, surface runoff (13 ± 3 mm per year) and subsurface runoff
1004 (11 ± 6 mm per year) show increasing trends of $+1.3$ and $+3.5$ mm per decade ($p=6 \times 10^{-5}$ and 3×10^{-7})
1005 respectively (Fig. 9B). The surface runoff presented on Fig. 9B includes the snow melt that did not
1006 infiltrate the ground. These linear trends we report are high compared to the absolute values of the
1007 variables and their extrapolation backward in time would lead to null values in the recent past which is
1008 unrealistic. This suggests a non-linear evolution of these variables over the XXth century.

1009 We also present the catchment average of the $runoff / (runoff + evaporation)$ ratio (Fig. 9C), which
1010 is equivalent to $runoff / (rain + snow - snow\ sublimation)$ given the negligible contribution of soil
1011 storage variations. Hence it is the proportion of the water input to the ground surface that is converted

a supprimé: 7C

a supprimé: 7D

a supprimé: 8A

a supprimé: 8B

a supprimé: 8B

a supprimé: 8B

a supprimé: 8C

1019 into runoff. This proportion is $11 \pm 2\%$ over the simulation time and shows an increasing trend of
1020 $+1.23\%$ per decade ($p=2 \times 10^{-7}$). Fig. 9C also shows the average theoretical ratio to maintain a steady
1021 lake level (of 17.6%). This ratio was obtained under the following hypothesis:

- 1022 • Same climate forcing data, hence same lake evaporation
- 1023 • The glacier contribution is (i) considered the same for the historical simulation and this
1024 scenario and (ii) taken as the difference between the total land surface runoff and the red
1025 curve of *required runoff* in figure 5, therefore independent of remotely sensed estimates.
- 1026 • Under these conditions, the runoff increase needed to maintain the lake level is only
1027 supplied by land runoff (surface and subsurface) by shifting the $runoff / (runoff +$
1028 $evaporation)$ ratio.

1029 The ratio from the historical simulation starts significantly below the theoretical steady lake ratio
1030 ($10.2\% < 17.6\%$, Fig. 9C) and increases progressively to 16.0% in 2019.

1031 Finally, Fig. 9D shows the annual proportion of *liquid / total* water averaged for the whole
1032 catchment. The value was computed based on the daily water content (liquid and frozen) of the first
1033 2 m of the soil column (the hydrologically active part of the column, Sect. 3.2.4) from which annual
1034 averages were derived and used to compute a catchment scale average. The graph indicates that the
1035 proportion of liquid water in the total water content increases at around $+1.41\%$ per decade ($p=1 \times 10^{-4}$),
1036 indicating an increasing availability of liquid water in the ground with time.

a supprimé: 8C

a supprimé: 8C

a supprimé: 8D

a supprimé:

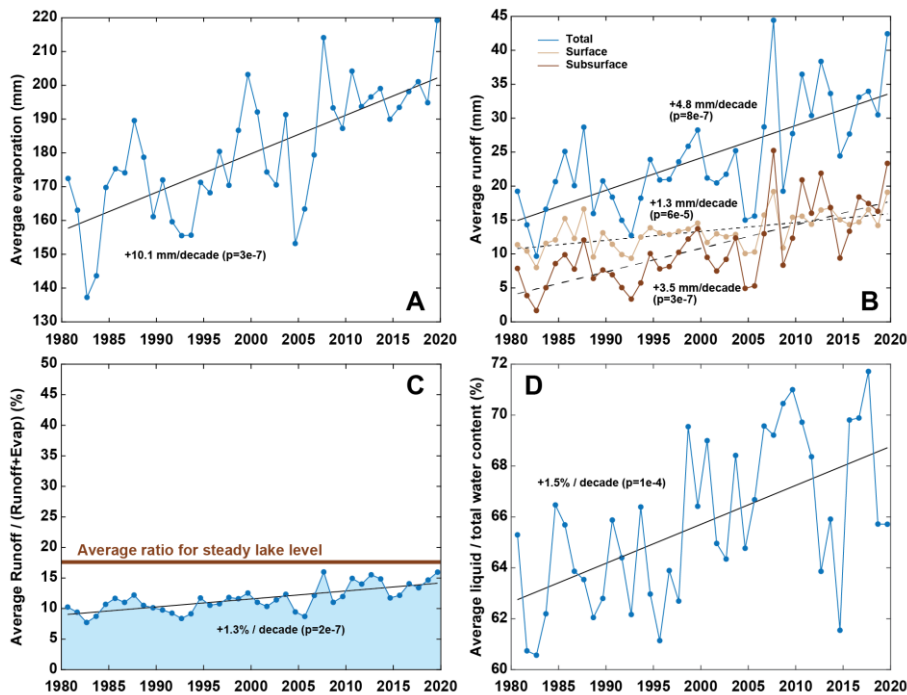


Figure 9. Hydrological results. A: Annual evaporation averaged over the whole catchment. B: Annual runoff averaged over the whole catchment. The blue curve sums the surface and subsurface runoff. C: Ratio between runoff and (evaporation + runoff) averaged over the whole catchment. The brown line indicates the theoretical average ratio needed to maintain a steady lake level when considering an identical glacier contribution to runoff (details in Sect. 4.3). D: Annual mean of the (liquid water)/(total water) ratio over the first 2 meters of ground, averaged over the whole catchment.

4.4. Sensitivity test on evaporation and runoff

We conducted a simple sensitivity test on the climatic conditions. We ran the same 40 years of simulations (with thermal initialization) for a climate 1 °C cooler and 30% wetter (more precipitation) than the historical scenario. We call this new scenario *colder and wetter* (to be compared with the *historical scenario*, i.e. the results of the present study presented in the rest of Sect. 4). Results of this experiment are presented in Fig. 10 and Table 2. Because of the difference in climate forcing, the *colder and wetter* scenario produced a greater amount of cold and warm permafrost areas than the historical scenario, as presented on Fig. 10A. Fig. 10B shows the proportion of the precipitation reaching the surface (rain + snow – snow sublimation) that produces runoff compared to evaporation for the Paiku catchment. Figure 10C aggregates over the whole catchment the distribution of such precipitation input

a supprimé: 8

a supprimé: Saut de page

¶ Hydrological budget of Lake Paiku¶
Our observations, climate data, simulations, geodetic data and the lake level data from Lei et al. (2018, 2021) enables us to quantify the different terms of the lake hydrological budget.

a déplacé (et inséré) [6]

a déplacé (et inséré) [7]

a déplacé (et inséré) [8]

a déplacé (et inséré) [9]

to the ground between runoff and evaporation for both scenarios. In between them, it also includes the distribution associated with the steady lake level scenario of Fig. 9C, which is based on the hypothesis listed as bullet points in Sect. 4.3 (climate forcing of the historical scenario, same glacier contribution, only land runoff increases).

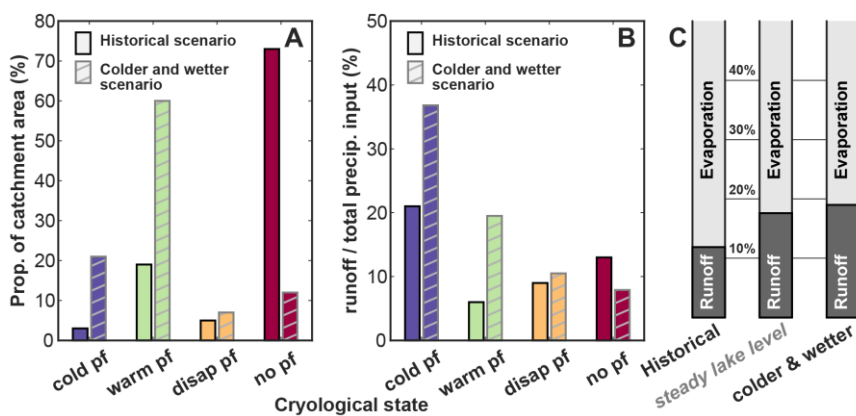


Figure 10. Sensitivity of the distribution between runoff and evaporation to climate. A: distribution of the different cryological states of the ground for the historical scenario (presented in Section 4) and for an alternative scenario where the climate is 1 °C colder and brings 30% more precipitation. B: runoff as a proportion of the precipitation input to the land (rainfall + snowfall – snow sublimation) for the different cryological states of the ground and for the 2 climatic scenarios. C: catchment scale ratio between runoff and evaporation for (i) the historical scenario, (ii) for a steady lake level with the same glacier contribution (same as Fig. 9C), and (iii) for the colder and wetter scenario.

The historical scenario shows that cold permafrost areas produce the highest proportion of runoff, which we attribute to the fact that the ground in these areas is most of the time frozen, turning a substantial part of the snow melt and rainfall into surface runoff. When considering grounds with a hydrologically active subsurface (warm permafrost, disappearing permafrost and no permafrost) in the historical scenario, the proportion of runoff increases slightly from warm permafrost to no permafrost. Such an evolution then corroborates the idea that the presence of permafrost tends to increase evaporation at the expense of runoff, as modeled by Sjöberg et al. (2021). Yet, for the colder and wetter scenario, runoff shows a regular decrease from cold to no permafrost with a more pronounced trend than the historical scenario. Several factors can be at play in this transition and most likely involve (i) a different extent and altitudinal distribution for each cryological type of ground, (ii) an overall reduced intensity of evaporation due to cooler surface temperatures, (iii) a higher soil water content driven by

a déplacé (et inséré) [10]

a mis en forme : Police : 11 pt

a déplacé (et inséré) [11]

a déplacé (et inséré) [12]

a déplacé (et inséré) [13]

higher precipitation and (iv) difference in the seasonal timings. Altogether, these processes substantially change the proportion of water that ends up as runoff water available for the lake, as highlighted by Fig. 10C.

Table 2. Distribution of between runoff and evaporation for the 2 scenarios

Ground cryological type	Historical Scenario			Colder and wetter scenario		
	Precipitation input ¹	Runoff	Evaporation	Precipitation input ¹	Runoff	Evaporation
Cold permafrost	100% 117 mm	21% 24 mm	79% 93 mm	100% 234 mm	37% 86 mm	63% 148 mm
Warm permafrost	100% 183 mm	6% 10 mm	94% 173 mm	100% 281 mm	20% 55 mm	80% 226 mm
Disappearing permafrost	100% 211 mm	9% 19 mm	91% 192 mm	100% 211 mm	10% 22 mm	90% 189 mm
No permafrost	100% 218 mm	13% 28 mm	87% 189 mm	100% 200 mm	8% 16 mm	92% 184 mm

¹. Precipitation input is the input to the ground, counted as rainfall + snowfall – snow sublimation.

a déplacé (et inséré) [14]

a supprimé: 9). As the unique output term, evaporation dominates the lake budget with an average annual value of 0.86 m (34.6 m / 40 years, Fig. 9A). Direct precipitation in the lake is the dominant input with an average annual value of 0.31 m (12.3 m / 40 years), followed by glacier runoff (0.28 m/yr, 11.3 m / 40 years) and land runoff (0.18 m/yr, 7.0 m / 40 years). When compared with lake volume observations over the 40 years of the simulation period, the simulated lake budget is 1.04 m too negative.

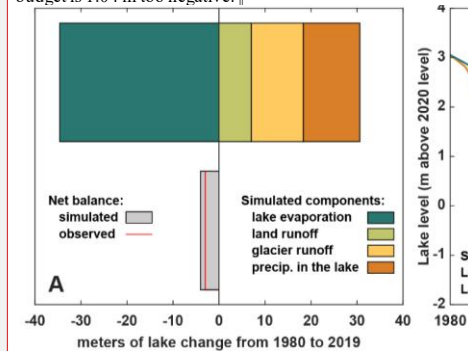


Figure 9.

a mis en forme : Retrait : Première ligne : 0 cm, Espace Avant : 0 pt

a déplacé vers le haut [1]: We present these results in m of lake level change based on the average slope of the Volume = f(level) relationship (Fig.

a déplacé vers le haut [2]: Budget and level of lake Paiku for the simulation period (1980-2019). A. The different components of the hydrological budget of the lake according to our framework. Results are given in m of lake change based on the average slope of the Volume = f(level) relationship. B. Lake level data. Points correspond to observations from Lei et al. (2018, 2021) that we smoothed (green curve, based also on observation points older than 1980). The simulated lake level appears in orange.

a déplacé vers le haut [3]: Based on our results, we also reconstructed lake level variations that we compare with the observed variations (Fig.

a déplacé vers le haut [4]:). Following our framework, our values are presented at an annual timestep. They qualitatively reproduce the overall lake level decrease but tend to overestimate this decrease and show an increasing mismatch with the observations from 0 in 1980 to 2 meters in 2005. This mismatch is later compensated by an increasing lake level trend in our simulation from 2005 to 2019. At the

a supprimé: 9A) and the fact that our approach provides 95% of the required runoff to close the lake budget (Sect. 4

a déplacé vers le haut [5]: .1.). This pattern of a too strong decrease followed by an increase is consistent with the comparison between simulated and required runoff presented on Fig. 5D.

a supprimé: 9B

a mis en forme : Police : +Corps(Calibri), 9 pt, Italique

1144 **5. Discussion**

1145 5.1. Limitation and potential of the approach

1146 *5.1.1. Data usage within the conceptual framework and data scarcity*

1147 Our approach relies on a variety of data regarding their scientific focus (glaciers, ground, lake,
1148 atmosphere), their type (in situ observations, remotely sensed data, reanalysis data), their characteristics
1149 (point wise data, distributed data, constant or with various time resolution) and the way they interact
1150 with our models (model parameters, forcing data, validation data, result data in case of the glacier
1151 runoff). Such a diversity arises from our goal to quantify both the ground thermo-hydrological regime
1152 and the different terms of the lake budget. This variety also makes it challenging to consistently merge
1153 these data into a unique framework. For example, our quantification of the glacier mass change
1154 reconstruction is made of two constant values for the study period (1975-2000 and 2000-2020), which
1155 limits the relevance of the comparison between the observed lake level variations and the simulated
1156 ones.

1157 Yet, the lake level variations are the only hydrological observations available to evaluate the
1158 robustness of the runoff we compute. Therefore, we had to combine lake level observations with our
1159 precipitation forcing data and lake evaporation quantifications in a simple mass conservation
1160 calculation, to derive the land runoff to the lake required to reproduce the level variations (red curve on
1161 Fig. 5D). In this regard, the sum of the glacier and land runoff we derive over the 40 years correspond
1162 to 95% of the required runoff to the lake, indicating that the magnitude of our reconstruction is correct.
1163 Year-to-year comparison is less accurate and we suggest that this is the consequence of the
1164 aforementioned limitations and also of our modeling strategy as detailed below.

1165 A main limitation regarding our usage of the data is related to the limited amount of available field
1166 observations required to provide robust model parameterizing, climate forcing and in-depth validation
1167 of the simulations, both hydrologically and thermally. Regarding climatic forcing data, our AWS
1168 measurement offers sound observations to evaluate and adjust the ERA5 data processed with TopoSUB
1169 and downscaled with TopoSCALE. Yet, a period of observations longer than 2 years would have
1170 enabled more robust corrections and could have allowed us to perform a more advanced statistical

1171 downscaling approach, e.g. quantile mapping (Thiemeßl et al., 2011). As such, the spatiotemporal
1172 domain of relevance of these corrections is insufficient to correct data for the whole catchment and the
1173 40 years of simulations. Overall, considering the strong bias we observe in the raw ERA5 data (Figure
1174 D1), these corrections do represent an important first-order improvement. Altogether, this scarcity of
1175 field observations is likely to bring significant uncertainties to our analysis. Future efforts should focus
1176 on acquiring additional data or developing validation methods based on remotely sensed observations.

1177 5.1.2. Modeling strategy

1178 By giving access to the timing of water transport across the catchment, water routing would allow
1179 to investigate temporal hydrological patterns at a monthly or seasonal scale. Because we work at annual
1180 and decadal time scales, this limitation has limited consequences on our results. The main consequence
1181 is to ignore potential storage effects on the land that would delay the arrival of runoff to the lake. We
1182 suggest that this limitation contributes to explaining the limited match between computed and required
1183 runoff at the annual time scale, (Fig. 5). Yet, our subdivision of the catchment based on the different
1184 cryological states of the ground allows us to work with hydrological units that are smaller than the
1185 catchment and thus present shorter hydrological response time to precipitation.

1186 Additionally, our approach regarding the modeling of runoff is relatively simple, i.e. partition
1187 between subsurface and surface runoff based on comparison between the soil water content and field
1188 capacity and porosity, respectively. More complex approaches split runoff into more sophisticated
1189 categories such as Horton overland flow, Dunne overland flow, subsurface stormflow... (e.g. Savenije,
1190 2010; Gao et al., 2014; Mirus and Loague, 2013). However, over the last decade, the relevance of this
1191 type of partitioning between different types of runoff has been questioned (McDonnell, 2013; Gao et
1192 al., n.d.). In the frame of our study, we find it important to distinguish between surface and subsurface
1193 runoff because they generate flows with very contrasted speed. In a general perspective, this significant
1194 difference in flow velocities impacts the hydrological system as a whole (e.g. river discharge,
1195 evaporation...) and has various consequences throughout the catchment, such as the water availability
1196 for vegetation, erosion and sediment transport.

a supprimé: quantile mapping (Thiemeßl et al., 2011). As such, the spatiotemporal domain of relevance of these corrections is insufficient to correct data for the whole catchment and the 40 years of simulations. Overall, considering the strong bias we observe in the raw ERA5 data (Figure D0), these corrections do represent an important first-order improvement

a supprimé: .

1205 In the particular case of a cryo-hydrological study, separating surface from subsurface runoff is
1206 particularly relevant because both flows do not react in the same way to ground temperature changes.
1207 As such, we see our approach as a middle way that allows us to make this distinction based on simple
1208 hydrological considerations. Yet, we acknowledge that the classification and quantification of the
1209 different types of runoff represent a valuable direction for future investigation on catchment-scale cryo-
1210 hydrology in Tibet. Another potential improvement in our modeling approach could be to unravel
1211 evaporation from transpiration. However, since vegetation is extremely scarce in the Paiku catchment,
1212 which is largely dominated by barren lands, we suggest that this would not significantly affect our
1213 results. However, this limitation should be explored in future field and modeling studies.

1214 Conversely, our approach also conveys several important advantages regarding our goal to
1215 describe and quantify the ground thermo-hydrological regime of the catchment. The use of TopoSUB
1216 enables us to produce results at a resolution of 100 x 100 m over an area of nearly 2400 km² with
1217 calculation costs 700 times lower than if each 100 x 100 m pixel was treated individually. Yet, thanks
1218 to the clustering method used to produce the forcing dataset (Sect. 3.2.2), the strong spatial variability
1219 of the physiography and its impact on the climate and incoming radiations is significant in the forcing
1220 data and has a major influence on the ground thermo-hydrological results, as exemplified by the strong
1221 spatial variability of ground temperatures (Fig. 7). Beyond elevation, other physiographic parameters
1222 such as aspect also influence the results. The mean values of 2 m-deep temperature and evaporation
1223 over the 40 years for north-facing areas (averaged over the whole catchment and over the 40 years) are
1224 1.3 °C and 163 mm while they reach 2.9 °C and 197 mm for the south-facing ones. This strong
1225 dependence of modeled results on physiography highlights the necessity to take it into account when
1226 modeling the thermo-hydrological regime of the ground in high mountainous environments. Finally,
1227 our approach allows us to couple the physical processes governing both energy and water fluxes at the
1228 surface and subsurface and highlight their interplay, as developed in section 5.1.4.

1229 *5.1.3. Reconstruction of the Lake hydrological budget and level variations*

1230 The total lake level change we simulate is a decrease of 4.11 m. This is qualitatively consistent
1231 with the overall observed trend. The mismatch with the observations is limited to a 1.06 m excess in

a supprimé: 6

1233 the simulated level drop (Fig. 9A). Our reconstruction shows a decrease of 4.66 m from 1980 to 2007,
1234 which is an overestimation of the initial drop. Afterwards, while observations indicate a gradual
1235 slowdown of the lake level decrease, we simulate a stabilization followed by a slight increase (0.55 up
1236 between 2013 and 2019).

1237 A possible reason for this mismatch is that the lake is connected to a larger aquifer that surrounds
1238 it. In the context of a decreasing lake level, an aquifer surrounding the lake can create an additional
1239 water inflow when the lake level passes below the piezometric level of the aquifer, (Yechieli et al.,
1240 1995). Such an inflow could mitigate the lake level decrease and thus explain the missing water in our
1241 reconstruction (Fig. 6B). It could also explain the gradual stabilization of the lake level that our model
1242 does not reproduce. This flow is not part of our conceptual hydrological framework even though it likely
1243 exists in reality, especially since there is no permafrost near the lake (as we simulate it here), allowing
1244 for the existence of such an aquifer (Walvoord and Kurylyk, 2016). Groundwater has been identified as
1245 a potential contributor to lake level rise in other regions of the QTP (Lei et al., 2022). In the long run,
1246 lake-aquifer systems commonly follow oscillations of the net atmospheric flux of water (Precipitation
1247 – Evaporation) and of the runoff that forces its mass balance (Watras et al., 2014). During these
1248 oscillations, the lake can “pump” water from the aquifer or feed it depending on the relative difference
1249 of piezometric level between them (Almendinger, 1990; Liefert et al., 2018). Yet, this potential effect
1250 is difficult to account for and its magnitude remains unclear. Therefore, the reasons for the mismatch
1251 between observed and simulated lake levels could also be connected to other aspects of our
1252 methodology such as bias in the climatic forcing data and other shortcomings arising from the lack of
1253 field data, or hydrological processes, as developed in Sect. 5.1.1 and 5.1.2.

1254 Our reconstruction of the lake budget is informative regarding the respective contribution of the
1255 different inputs and outputs. Regarding lake evaporation, our mean value of 870 ± 23 mm is close to
1256 the one modelled by Yang et al. (2016) with the Flake model for lake Nam (832 ± 69 mm) for the period
1257 1980-2014 but we do not report a significant increasing trend in our results. Yet for the same lake (Nam
1258 Co) and a similar period (1980-2016) Zhong et al., (2020) reported an average value of 1149 ± 71 mm
1259 (along with an increasing temporal trend) using the Penman formula (Penman, 1948), thus highlighting
1260 the potential dependence of the results to the methodology. In our results, direct precipitation to the lake

a supprimé: .

a supprimé: .

a supprimé: (Walvoord and Kurylyk, 2016). Ground water has been identified as a potential contributor to lake level rise in other regions of the QTP (Lei et al., 2022).

a supprimé: Regarding lake evaporation, our mean value of 870 ± 23 mm is close to the one modelled by Yang et al. (2016) with the Flake model for lake Nam (832 ± 69 mm) for the period 1980-2014 but we do not report a significant increasing trend in our results. Yet for the same lake (Nam Co) and a similar period (1980-2016) Zhong et al. (2020) reported an average value of 1149 ± 71 mm (along with an increasing temporal trend) using the Penman formula (Penman, 1948), thus highlighting the potential dependence of the results to the methodology. In our results, direct precipitation to the lake represents 40% of the inputs, followed by glacial runoff (35%) and land runoff (25%). Glaciers are therefore a particularly important contributor to the runoff towards the lake (60% of the total runoff, vs. 40% for land runoff), what contrasts with the results from Biskop et al. (2016) who calculated that the runoff input to the lake Paiku was dominated by land runoff (70% and 30% for the glacier contribution). Here again, these difference likely arises from important differences in input data and methodologies to quantify the different hydrological processes (evaporation, runoff, snow and glacier melt). Yao et al., (2018) reported that, at the QTP scale, the balance between precipitation and evaporation (over land and lake) was dominant over glacier melt to understand both lake storage increases and decreases. Our reconstruction does not give us access to significant temporal variation of the glacier contribution but the above-mentioned proportions in the contributions to the lake (40%, 35% and 25%) show that the glacier contribution does not dominate the input terms. At the catchment scale, these proportions can vary significantly depending on the glacier coverage. For Lake Selin, Zhou et al. (2015) reported that runoff towards the lake, evaporation from the lake and on-lake precipitation altogether explained 90% of the lake storage variations for the 2003-2012 period. The catchment of lake Selin exhibits a very limited glacier coverage (0,63% of its area, Lei et al., 2013)

1302 represents 40% of the inputs, followed by glacial runoff (35%) and land runoff (25%). Glaciers are
1303 therefore a particularly important contributor to the runoff towards the lake (60% of the total runoff, vs.
1304 40% for land runoff), what contrasts with the results from Biskop et al. (2016) who calculated that the
1305 runoff input to the lake Paiku was dominated by land runoff (70% vs. 30% for the glacier contribution).
1306 Here again, these difference likely arises from important differences in input data and methodologies
1307 to quantify the different hydrological processes (evaporation, runoff, snow and glacier melt). Yao et al.
1308 (2018) reported that, at the QTP scale, the balance between precipitation and evaporation (over land
1309 and lake) was dominant over glacier melt to understand both lake storage increases and decreases. Our
1310 reconstruction does not give us access to significant temporal variation of the glacier contribution but
1311 the above-mentioned proportions in the contributions to the lake (40%, 35% and 25%) show that the
1312 glacier contribution does not dominate the input terms. At the catchment scale, these proportions can
1313 vary significantly depending on the glacier coverage. For Lake Selin, Zhou et al. (2015) reported that
1314 runoff towards the lake, evaporation from the lake and on-lake precipitation altogether explained 90%
1315 of the lake storage variations for the 2003-2012 period. The catchment of lake Selin has a very limited
1316 glacier coverage, corresponding to 0.63% of its area (Lei et al., 2013), compared to the Paiku (5%).

1317 5.1.4. *The interdependence of thermal and hydrological variables*

1318 Our simulation results enable us to explore the interplay between the fluxes of energy and water at
1319 the surface and subsurface. In this regard, we tested the correlation of evaporation with the proportion
1320 of liquid/total water in the ground for cold and warm permafrost, as well as the correlation between
1321 evaporation and the duration of seasonal thaw at a 70 cm depth (Fig. 11, A and B). For permafrost areas
1322 (*cold permafrost* and *warm permafrost*), evaporation shows a strong correlation with the seasonal
1323 distribution between liquid and frozen water, similar to previous modeling works for the region (Cuo
1324 et al., 2015). As such, this correlation suggests that the intensity of seasonal ground thaw plays a role
1325 in enabling higher or lower evaporative fluxes. This is likely due to cold surface temperatures strongly
1326 reducing water loss from the surface and because moisture delivery to the surface is inhibited when the
1327 ground is frozen. We suggest that this dependence is particularly important in the Paiku Catchment
1328 because evaporation is strong (88% of the precipitation input to the surface evaporates on average) and

a supprimé: 10A

a supprimé: (Cuo et al., 2015).

1331 because frozen water is the dominant form of water in the ground in permafrost areas (Fig. 11A, the
1332 calculation includes the first 2 meters below the surface).

a supprimé: 10A

1333 Similarly, evaporation in *no permafrost* areas shows a significant correlation with the duration of
1334 the seasonal thaw (Fig. 11B). We suggest that this result arises from the fact that frozen ground limits
1335 the evaporative fluxes and thus years during which the subsurface seasonal thaw is shorter are associated
1336 with reduced evaporative fluxes. We also tested the relationship between the linear trend of active layer
1337 deepening and the mean evaporation (over the 40 years of simulation) for *warm permafrost* areas (Fig.

a supprimé: 10B

1338 11C). Thus, this graph does not present annual values and one point corresponds to one of the 92
1339 TopoSUB points classified as *warm permafrost* (values averaging the 40 years). The graph highlights
1340 that TopoSUB points showing an Active Layer (AL) deepening trend are associated with low
1341 evaporation and precipitation. From there, TopoSUB points with stronger evaporation show no
1342 deepening trend or even a shrinkage of the AL. This relationship is contradicted by the highest level of
1343 evaporation (>240 mm per year) observed for *warm permafrost*, for which AL deepening is observed
1344 again (dark blue points of the graph). These TopoSUB points with the highest levels of evaporation also
1345 correspond to those receiving the largest amount of precipitation. Further discussion on active layer
1346 trends is provided in the next section.

a supprimé: 10C

a supprimé: based on

1347 Runoff also shows a strong connection with the ground thermal regime (Fig. 11D). At the
1348 beginning of the simulation, years with an average 2 m-deep temperature below 0 °C are associated
1349 with limited subsurface runoff (< 5 mm per year). Over the years, as the ground warms up and
1350 permafrost disappears, subsurface runoff increases and can reach 20 to 45 mm per year. This result is
1351 consistent with increased subsurface connectivity expected when permafrost thaws (Kurylyk et al.,
1352 2014; Gao et al., 2021) that has been both observed (Niu et al., 2016) and modeled (Lamontagne-Hallé
1353 et al., 2018; Huang et al., 2020; Gao et al., 2018). We suggest that these substantial changes in
1354 subsurface runoff, associated with changes in the ground temperature in Fig. 11D support the hypothesis
1355 of a modification in the hydrological pathways as permafrost thaws.

a supprimé: 10D). At the beginning of the simulation, years with an average 2 m-deep temperature below 0 °C are associated with limited subsurface runoff (< 5 mm per year). Over the years, as the ground warms up and permafrost disappears, subsurface runoff increases and can reach 20 to 45 mm per year. This result is consistent with increased subsurface connectivity expected when permafrost thaws (Gao et al., 2021; Kurylyk et al., 2014) that has been both observed (Niu et al., 2016) and modeled (Gao et al., 2018; Huang et al., 2020; Lamontagne-Hallé et al., 2018). We suggest that these substantial changes in subsurface runoff, associated with changes in the ground temperature in Fig. 10D...

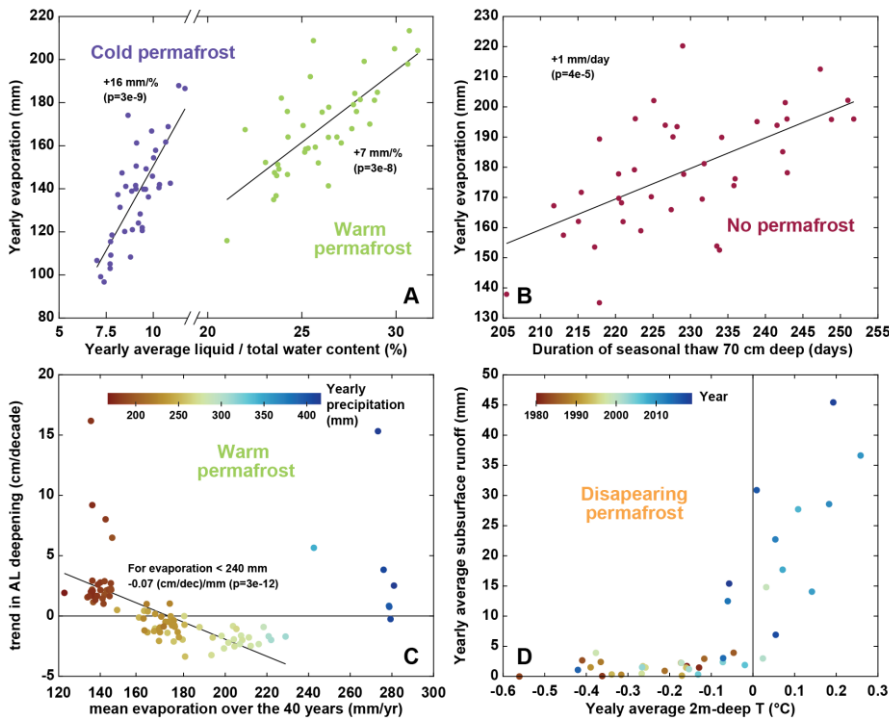


Figure 11. Thermo-hydrological couplings. A: Annual evaporation vs. annual mean of the liquid / total water ratio over the first 2 meters of ground, averaged for simulations corresponding to cold permafrost and warm permafrost (one dot per year for each permafrost category). B: Annual evaporation vs. duration of seasonal thaw at a 70 cm depth averaged for simulations corresponding to locations without permafrost (one dot per year). C: Active layer deepening trend vs. mean evaporation over the 40-year for each simulation corresponding to warm permafrost (here one dot corresponds to one TopoSUB point). The color of the dots shows the precipitations averaged over the 40 years for each simulation. The linear regression excludes simulations exhibiting annual evaporation higher than 240 mm. D: Annual subsurface runoff vs Annual 2 m-deep temperature averaged for simulations corresponding to locations with disappearing permafrost (one dot per year). The color of the dot indicates the year of the simulation.

a supprimé: 10

Altogether, these results suggest a dependence of key variables quantifying the catchment hydrological balance (evaporation, runoff) to the seasonal characteristics and interannual trends of the ground thermal regime (temperature, liquid vs frozen water content). Similar to previous studies (Ding et al., 2020; Wang and Gao, 2022), we think these results advocate for the necessity to couple thermal and hydrological modeling to improve our ability to understand and quantify changes in the hydrological balance of high mountain catchments. To our best knowledge, along with Gao et al. (2022), our study represents to date the most complete effort to include the variety of coupled climatological,

a supprimé: Similar to previous studies (Ding et al., 2020; Wang and Gao, 2022), we think these results advocate for the necessity to couple thermal and hydrological modeling to improve our ability to understand and quantify changes in the hydrological balance of high mountain catchments. To our best knowledge, along with Gao et al. (2022),

1400 surface and subsurface processes characterizing the climate, hydrology and ground thermal regime of
1401 high-mountain catchments in Tibet at a small scale with a high spatial resolution.

1402 5.2. Cryo-hydrological trends in the catchment and across the QTP

1403 5.2.1. Permafrost and ground temperature changes

1404 Our results indicate that permafrost coverage in the Paiku catchment evolved from 27 to 22% of
1405 the land area during the simulated period. Such a coverage corresponds to sporadic permafrost (10-50%
1406 of the area) and is consistent with recent large-scale estimates of permafrost in the Northern Hemisphere
1407 (Obu et al., 2019) and across the QTP (Zou et al., 2017; Ran et al., 2018). This decrease corresponds to
1408 a 19% shrinkage of the 1980 permafrost area, which is higher than the 9% reported by Gao et al. (2018),
1409 a value determined by catchment-scale numerical modeling in the upper Heihe catchment (northeastern
1410 QTP) over a similar period. It is also slightly higher than the 13% decrease modeled from 1971 to 2015
1411 for the Qinghai Lake catchment with a similar approach by Wang and Gao (2022). Yet, it is smaller
1412 than the 34% loss modeled by Qin et al. (2017) from 1981 to 2015 for the Yellow River Source Region
1413 (YRSR, North Eastern QTP).

1414 Active layer (AL) evolution is contrasting throughout the catchment and a deepening signal is only
1415 visible for the locations with limited evaporation (<150 mm per year). Given the strong drive of summer
1416 climate on Active Layer Thickness (ALT), this overall lack of a deepening trend highlights how
1417 evaporation can act as an energy intake at the surface (Yang et al., 2014a), limiting the surface and
1418 subsurface heat fluxes and thus AL deepening. In this regard, our results fall in line with the conclusions
1419 of Fisher et al. (2016) when observing evapotranspiration and ALTs in boreal forests and also confirm
1420 the modeling experiments of Zhang et al. (2021b) on permafrost wetting in arid regions of the QTP.
1421 Besides, the lack of an overall deepening trend is consistent with observations from Luo et al. (2018)
1422 in the YRSR over the last decade and with the modeled AL from Zhang et al. (2019) at the scale of the
1423 QTP for the last 40 years. Where evaporation is limited, we report an AL deepening trend of 2.7 cm per
1424 decade, which is smaller than the 4.8 cm per decade trend modeled by Song et al. (2020) for the YRSR

a déplacé (et inséré) [15]

a mis en forme : Espace Avant : 54 pt

a déplacé (et inséré) [16]

1425 for the same period, and smaller than the 4.3 cm modeled by Gao et al (2018) in the upper Heihe
1426 catchment. Yet it is comparable to the 2 cm per decade value modeled by Wang and Gao (2022) for the
1427 Qinghai Lake catchment from 1971 to 2015.

1428 In no permafrost areas, our simulations show that the thickness of seasonally frozen ground shrinks
1429 at a rate of 6.8 cm per decade. This rate is faster than the rate of 3.1 cm per decade quantified by Qin et
1430 al. (2018) using the Stefan solution for the YRSR (1961-2016) and faster than the 3.2 cm per decade
1431 modeled by Gao et al. (2018, Heihe catchment). However, it is similar to the 6 cm per decade rate
1432 modeled by Wang and Gao (2022) in the Qinghai Lake catchment from 1971 to 2015 and smaller than
1433 the 12 cm per decade modeled by Qin et al. (2017) for the YRSR (1981-2015). All these values fall
1434 within the wide range of 3 to 29 cm per decade reported by Wang et al. (2020a) when studying
1435 seasonally frozen ground over the whole QTP with in-situ observations. Regarding timing, we report a
1436 decreasing trend of 5.3 days of frozen conditions (70 cm deep) per decade which is consistent with the
1437 decrease of 6.7 days per decade reported by Wang et al. (2020a) just below the surface.

1438 Regarding the timing of seasonal ground thaw, our results highlight that the increase in the duration
1439 in the seasonal ground thaw (at 70 cm) is mostly driven by a progressive delay of the end date of the
1440 thaw period. This result contrasts with those from Song et al. (2020) for the same period in the YRSR
1441 who also modeled an increase of the seasonal thaw (at a 2 cm depth), although driven by an advancing
1442 trend of the start date of the seasonal thaw.

1443 Our warming trends at a 4 m depth for permafrost areas is 0.1 °C per decade, which is substantially
1444 smaller than the 0.43 °C per decade observed at this depth between 1996 and 2006 in permafrost
1445 boreholes along the Qinghai-Tibetan Highway in the North East of the QTP (Wu and Zhang, 2008).
1446 Zhang et al. (2019) reported a 0.13 °C per decade of warming of the permafrost top during winter that
1447 is consistent with the trend of 0.14 °C per decade we observe at 2 m depth (mean AL between 1.4 and
1448 1.7 m in our simulations) for the months of December, January and February.

1449 5.2.2. Evaporation and runoff changes

1450 Our results are characterized by (i) an increase of both evaporation and runoff (Fig. 9A and 9B),
1451 mainly driven by an increase in precipitation (Fig. 3 bottom), (ii) a runoff/(runoff+evaporation) ratio

a déplacé (et inséré) [17]

1452 exhibiting an increasing trend as a result of ground warming and permafrost disappearance that both
1453 enable more subsurface runoff along time (Fig. 9C and 10D) and (iii) an increase in the proportion of
1454 liquid water in the ground compared to ice (Fig. 9D). Regarding all these points, our results find a good
1455 consistency with the evolution reported by Gao et al. (2018) for the upper Heihe catchment
1456 (northeastern QTP) using a similar approach for a comparable period (1971-2013). The increasing
1457 trends in evaporation and runoff they report for the thawing season (dominant period for both processes)
1458 are comparable with the annual values we report: +10.0 mm per decade for evaporation (our study:
1459 +10.1 mm per decade) and +3.3 mm per decade for runoff (our study: +4.8 mm per decade). Similar
1460 evolutions are also reported by Wang and Gao (2022) for the Qinghai Lake catchment and by Qin et al.
1461 (2017) for the YRSR (1981-2015). These increases in runoff (especially surface runoff) are likely to
1462 have an influence on sediment transport. For instance, Li et al. (2021) showed that current precipitation
1463 augmentation over High Mountain Asia is driving a runoff increase, which contributes to a significant
1464 rise in fluvial sediment fluxes. Regarding differences, Qin et al. (2017) modeled a stronger evaporation
1465 increase (14.3 mm per decade) linked to a decreasing runoff coefficient. Similar to Li et al. (2019), we
1466 see that an important part of snow melt (49%) infiltrates the ground and later contributes to runoff and
1467 evaporation.

1468 5.3. Evaporation vs runoff and sensitivity to climate conditions

1469 Our results indicate that evaporation is particularly strong in the Paiku catchment. Over the 40
1470 years of simulation, 10% of the total precipitation is converted into runoff, and the rest of the water is
1471 either directly returned to the atmosphere from the snowpack via snow sublimation or from the ground
1472 surface via evaporation. Comparatively, Gao et al. (2018) observed and modeled a ratio of around 35%
1473 for the Heihe catchment; Qin et al. (2017) reported an average ratio of 33% for the YRSR and Li et al.
1474 (2014), a ratio of 83% for the Qugaqie catchment (central QTP) but modeling hydrological fluxes only.
1475 Our sensitivity test on evaporation and runoff for a slightly different climates (Sect. 4.4) highlights
1476 the fact that the role of permafrost regarding the runoff/evaporation distribution is a complex question.

a déplacé (et inséré) [18]

as it has already been discussed in the literature (e.g. Bring et al., 2016). Some studies have suggested that landscape-scale permafrost thaw would trigger more evaporation (Walvoord and Kurylyk, 2016). This phenomenon was modeled by Wang et al. (2018) in the upper Heihe River Catchment, for which they reported that the thickening of the active layer increased the ground storage capacity and led to a decrease in runoff and an increase in evapotranspiration. Wang et al. (2020b) also reported that permafrost thawing accelerated evapotranspiration (1961-2014).

Conversely, Zhang et al. (2003) and Carey and Woo (1999) reported that shallow frozen ground conditions (such as a shallow active layer) maintain higher water contents close to the surface, promoting higher evaporation. Sjöberg et al. (2021) modeled this phenomenon with a fully coupled cryo-hydrological model including surface energy balance calculation. They modeled a slope with a simplified geometry in 2D for different permafrost coverages. They found that hillslopes with continuous permafrost have twice as high rates of evapotranspiration compared to hillslopes with no permafrost.

As such, the interplay between the runoff/evaporation distribution and the ground thermal regime in areas where permafrost coverage shows a spatiotemporal variability is difficult to apprehend (Fig 10). This complexity is most likely due to a strong sensitivity to the drainage conditions (fast flows of steep mountain environments vs. slow flows of lowland catchments) and to the climate setting, both at the annual scale (arid regions vs. wet regions) and at the seasonal time scale (relative timing of temperature variations, rainfall, snowfall, snow melt and ground freeze/thaw).

Because it can both promote evaporation or runoff depending on the setting, the ground thermal regime of the catchment seems to have the possibility to create a positive feedback, both towards lake level decrease or increase. Further studies should therefore focus on comparing the thermo-hydrological regime of different Tibetan catchments with contrasting lake level changes and permafrost coverage, to test to which extent these differences can contribute to explain the spatial patterns of lake level changes across the QTP.

a déplacé vers le haut [15]: Cryo-hydrological trends in the catchment and across the QTP¶
Permafrost and ground temperature changes¶

a déplacé vers le haut [16]: Yet, it is smaller than the

a déplacé vers le haut [9]: Fig.

a déplacé vers le haut [18]: runoff, and the rest of the

a supprimé: Such a coverage corresponds to sporadic

a supprimé: Given the strong drive of summer climate

a supprimé: 8A and 8B

a déplacé vers le haut [17]:), mainly driven by an

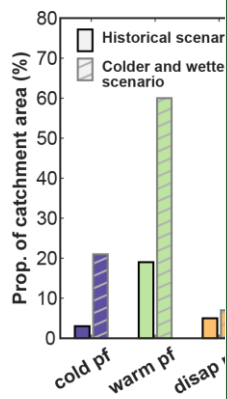
a supprimé: 8C and 10D) and (iii) an increase in the

a supprimé: (2017) reported an average ratio of 33% if

a déplacé vers le haut [6]: We ran the same 40 years of

a déplacé vers le haut [8]: Because of the difference in

a supprimé: 11A. Fig. 11B shows the proportion of the



a déplacé vers le haut [10]:

a supprimé: 11.

a déplacé vers le haut [11]: Sensitivity of the distribution

a supprimé: To further understand this question in the ca

a déplacé vers le haut [13]: Yet, for the colder and

a supprimé: Sect.

a déplacé vers le haut [7]: 4). Results of this experiment

a mis en forme : Police :11 pt

a supprimé: 8C

a supprimé: Such an evolution then corroborates the idea

a déplacé vers le haut [12]:), and (iii) for the colder and

a supprimé: Several factors can be at play in this transitid

a déplacé vers le haut [14]: Altogether, these processes

a supprimé: 11.

a supprimé: 11C.¶

a mis en forme : Police :Non Italique

1751 6. Conclusion

1752 We confirm that the Paiku catchment presents different types of ground cryological states from
1753 seasonally frozen ground to permafrost. Permafrost coverage shrinks from 27 to 22% of the land area
1754 of the catchment from the 1980s to the 2010s (19% loss of the 1980 permafrost area). The whole
1755 catchment warms up at a rate of 0.17 °C per decade (2 m deep), with a substantial elevation-dependent
1756 variability. This warming is concomitant with an increase in the duration of the seasonal thaw, mainly
1757 supported by a progressive delay of the end date of the thaw period. Where permafrost is present, active
1758 layer deepening is only observed where evaporation is relatively low (<150 mm yr⁻¹).

1759 Over the simulation period, we also report an increase in evaporation (+10.1 mm per decade),
1760 surface and subsurface runoff (+1.3 and +3.5 mm per decade respectively). Together, this leads towards
1761 an increase of the runoff/(runoff+ evaporation) ratio of +1.2% per decade. These results highlight the
1762 strong interdependence between the ground thermal and hydrological regimes and the necessity to
1763 jointly represent them to accurately quantify evaporation and runoff in this type of environment.

1764 In regard of lake level variations, the results we present highlight that:

- 1765 • The sum of the direct precipitation in the lake, the land runoff and the glacier runoff are not enough
1766 to compensate for the lake evaporation over the study period, hence driving the observed lake level
1767 decrease.
- 1768 • Long-term hydrological trends in the catchment are led by trends in climate; and precipitation
1769 increase, jointly with glacier melt, provides enough water to drive a concomitant increase of runoff
1770 and evaporation.
- 1771 • Ground thermal changes increase the distribution of liquid vs. frozen water in the ground and the
1772 duration of seasonal thaw, correlations suggest that these modifications increase evaporation. The
1773 warming of the ground is also related to the increase of subsurface runoff towards the lake.
- 1774 • Ground warming and permafrost thawing promote subsurface runoff over time, contributing to an
1775 increase in the runoff/evaporation ratio of the catchment.
- 1776 • Over the 40 years we studied, the presence of permafrost seems to promote evaporation at the
1777 expense of runoff. Yet this trend appears to be climate-dependent and the cryological state of the

a supprimé: last

1779 ground might shift the runoff/evaporation distribution in the other direction under colder and wetter
1780 climates.

1781 At the scale of the QTP, these results have several implications. First, a better understanding of the
1782 recent and future lake level variations will come with a better knowledge of spatial patterns and
1783 temporal trends in precipitation. Second, climate changes are modifying the ground thermal regime of
1784 Tibetan catchments through active layer deepening and changes in the seasonal freeze/thaw cycles,
1785 affecting evaporation, runoff volumes and pathways and overall, changing the hydrological functioning
1786 of Tibetan catchments (and the waterflow provided to the lakes). Finally, the effect of permafrost on
1787 the distribution between evaporation and runoff seems to be dependent on the climate settings and the
1788 permafrost coverage of the catchment. Further studies should investigate this phenomenon and how it
1789 might contribute to explaining the contrasting lake level evolutions across the QTP.

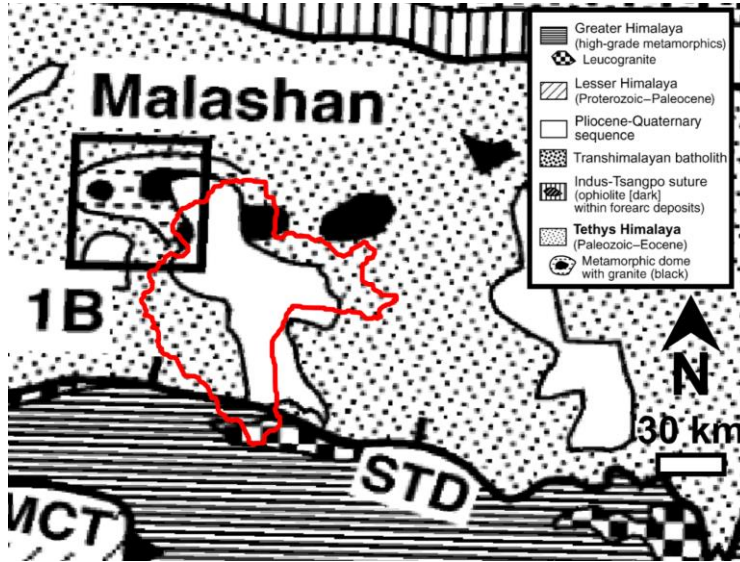
1790 **Appendix A: model parameters**

1791 *Table A1. Parameters of the model.*

Depth	Layer	Parameter	Values	Source	Calculation
0.0 m	Surface	Albedo	0.24	Modis MCD43A3.006	November mean, 4600-5100 masl
		Emissivity	0.95	Modis MCD43A3.006	November mean, 4600-5100 masl
		Roughness	0.024	-	Adjusted to fit loggers T values
0.0 m		Thickness	0.30 m	HiHydro Soil v1.0	modeling framework
		Porosity	0.5	Shangguann et al. 2013	mean
		Organic	8.60%	HiHydro Soil v1.0	catchment mean
0.3 m	Top soil	Mineral	41.40%	-	subtraction (100 - porosity - orga)
		Soil type	Sand	Shangguann et al. 2013	dominant fraction
		Field capacity	0.32	HiHydro Soil v1.0	catchment mean
0.3 m		Hydro cond	0.000030 m s ⁻¹	HiHydro Soil v1.0	catchment mean
		Alpha	0.028 cm ⁻¹	HiHydro Soil v1.0	catchment mean
		n	1.481	HiHydro Soil v1.0	catchment mean
0.3 m		Thickness	1.70 m	Shangguan et al. 2017	truncation, consistent with literature
		Porosity	0.4	Shangguann et al. 2013	catchment mean
		Organic	4.20%	HiHydro Soil v1.0	catchment mean
1.7 m	Bottom soil	Mineral	55.80%	-	subtraction (100 - porosity - orga)
		Soil type	Sand	Shangguann et al. 2013	dominant fraction
		Field capacity	0.32	HiHydro Soil v1.0	catchment mean
2.0 m		Hydro cond	0.000016 m s ⁻¹	HiHydro Soil v1.0	catchment mean
		Alpha	0.062 cm ⁻¹	HiHydro Soil v1.0	catchment mean
		n	1.707	HiHydro Soil v1.0	catchment mean
2.0 m		Thickness	98.3 m	-	-
		Porosity	0.03	-	-
98 m	Bedrock	Organic	0%	-	-
		Mineral	97%	-	-
100 m		Soil type	Sand	-	-
		Field Capacity	0.03	-	equal to porosity

1792

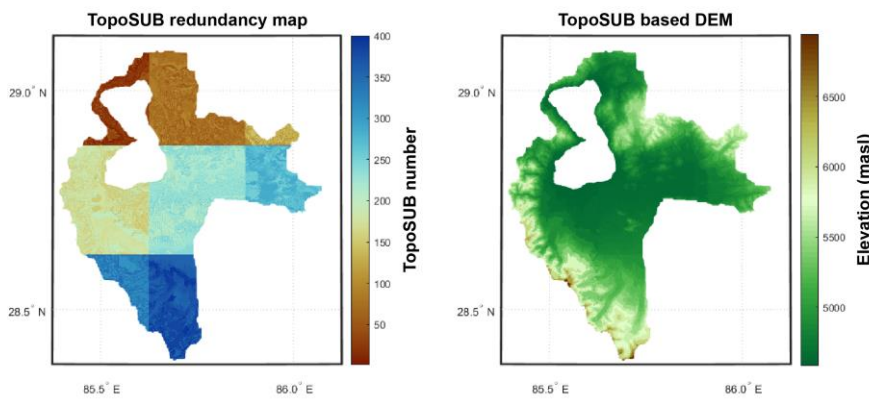
1793 **Appendix B: Geological map of the catchment**



1794
1795 Figure B1. Geology of the catchment. Modified from Aoya et al. (2015). The red contour indicates the
1796 limits of the Paiku catchment.

a supprimé: B0

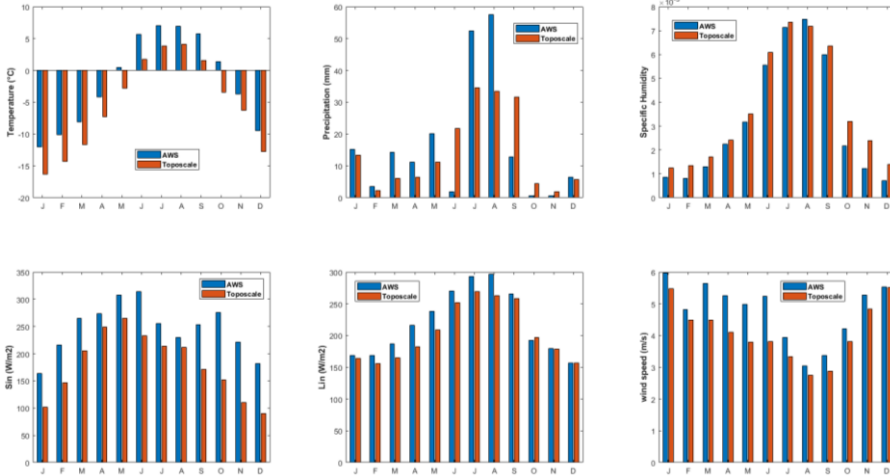
1797 **Appendix C: TopoSUB subsampling of the catchment**



1798
1799 Figure C1. Application of the TopoSUB clustering method (Fiddes and Gruber, 2012) in the Paiku
1800 catchment. Left: number of the TopoSUB points. Strong color changes reflect the footprint of the 8
1801 ERA5 pixels that the catchment intersects. Small color changes within a given of these zones show the
1802 distribution of the 50 TopoSUB points covering each tile (Sect. 3.2.2.) B: topographic map
1803 reconstructed using the TopoSUB approach.

a supprimé: C0. Application of the TopoSUB clustering method (Fiddes and Gruber, 2012) in the Paiku catchment.

1807 **Appendix D: Evaluation of forcing data**



1808
 1809 **Figure D1.** Comparison between the AWS data and the model forcing data downscaled from ERA5 with
 1810 the TopoSCALE and TopoSUB approaches. Based on the AWS data, a monthly correction factor is
 1811 applied to the downscaled data so that monthly data matches for the observed period for each variable
 1812 (methodological details in Sect. 3.2.2.).

a supprimé: D0

Code availability. The CryoGrid community model (version 1.0) and related documentation are available at: https://github.com/CryoGrid/CryoGridCommunity_source.

Data availability. Field data have been saved on Zenodo.org and will be published with a DOI upon acceptance of the manuscript.

Author contribution. L.M, W. I. and S.W. designed the study. L.M. and M.M. conducted the numerical simulations. S.W., M.L. and L.M. contributed to the model development. F.B., W.I., Y.L. ad S.A. acquired field data. L.M., F.B., M.M., P.K., Y.L. and T.M. analyzed and processed the data. J.F. provided downscaled forcing data for the model. All authors contributed to result interpretation and to manuscript preparation.

Competing interests. The authors declare that they have no conflict of interest.

Acknowledgements. This study was funded by the open program of the Dutch Research Council (NWO) (ALWOP.467) and by the Strategic Priority Research Program of the Chinese Academy of Sciences within the Pan-Third Pole Environment framework (grant agreement no. XDA20100300). The land surface and lake simulations were performed on Utrecht Geosciences computer cluster. Sebastian Westermann acknowledges funding by European Space Agency Permafrost_CCI (<https://climate.esa.int/en/projects/permafrost/>). We are very grateful to the reviewers for their input which significantly improved this manuscript.

a mis en forme : Couleur de police : Automatique
a supprimé:
a mis en forme : Couleur de police : Automatique

a mis en forme : Centré, Retrait : Première ligne : 0 cm
a mis en forme : Police : 10 pt, Gras

References

- Almendinger, J. E.: Groundwater control of closed-basin lake levels under steady-state conditions, *J Hydrol (Amst)*, 112, 293–318, [https://doi.org/10.1016/0022-1694\(90\)90020-X](https://doi.org/10.1016/0022-1694(90)90020-X), 1990.
- Aoya, M., Wallis, S. R., Terada, K., Lee, J., Kawakami, T., Wang, Y., and Heizler, M.: North-south extension in the Tibetan crust triggered by granite emplacement, *Geology*, 33, 853, <https://doi.org/10.1130/G21806.1>, 2005.
- Bhattacharya, A., Bolch, T., Mukherjee, K., King, O., Menounos, B., Kapitsa, V., Neckel, N., Yang, W., and Yao, T.: High Mountain Asian glacier response to climate revealed by multi-temporal satellite observations since the 1960s, *Nat Commun*, 12, 4133, <https://doi.org/10.1038/s41467-021-24180-y>, 2021.
- Bibi, S., Wang, L., Li, X., Zhou, J., Chen, D., and Yao, T.: Climatic and associated cryospheric, biospheric, and hydrological changes on the Tibetan Plateau: a review, *International Journal of Climatology*, 38, e1–e17, <https://doi.org/10.1002/joc.5411>, 2018.
- Biskop, S., Maussion, F., Krause, P., and Fink, M.: Differences in the water-balance components of four lakes in the southern-central Tibetan Plateau, *Hydrol Earth Syst Sci*, 20, 209–225, <https://doi.org/10.5194/hess-20-209-2016>, 2016.
- Bolch, T., Shea, J. M., Liu, S., Azam, F. M., Gao, Y., Gruber, S., Immerzeel, W. W., Kulkarni, A., Li, H., Tahir, A. A., Zhang, G., and Zhang, Y.: Status and Change of the Cryosphere in the Extended Hindu Kush Himalaya Region, in: *The Hindu Kush Himalaya Assessment: Mountains, Climate Change, Sustainability and People*, edited by: Wester, P., Mishra, A., Mukherji, A., and Shrestha, A. B., Springer International Publishing, Cham, 209–255, https://doi.org/10.1007/978-3-319-92288-1_7, 2019.
- Bring, A., Fedorova, I., Dibike, Y., Hinzman, L., Mård, J., Mernild, S. H., Prowse, T., Semenova, O., Stuefer, S. L., and Woo, M. -K.: Arctic terrestrial hydrology: A synthesis of processes, regional effects, and research challenges, *J Geophys Res Biogeosci*, 121, 621–649, <https://doi.org/10.1002/2015JG003131>, 2016.
- Brun, F., Berthier, E., Wagnon, P., Kääb, A., and Treichler, D.: A spatially resolved estimate of High Mountain Asia glacier mass balances from 2000 to 2016, *Nat Geosci*, 10, 668–673, <https://doi.org/10.1038/ngeo2999>, 2017.
- Brun, F., Treichler, D., Shean, D., and Immerzeel, W. W.: Limited Contribution of Glacier Mass Loss to the Recent Increase in Tibetan Plateau Lake Volume, *Front Earth Sci (Lausanne)*, 8, 1–14, <https://doi.org/10.3389/feart.2020.582060>, 2020.
- Cao, J., Qin, D., Kang, E., and Li, Y.: River discharge changes in the Qinghai-Tibet Plateau, *Chinese Science Bulletin*, 51, 594–600, <https://doi.org/10.1007/s11434-006-0594-6>, 2006.
- Carey, S. K. and Woo, M.: Spatial variability of hillslope water balance, wolf creek basin, subarctic yukon, *Hydrol Process*, 15, 3113–3132, <https://doi.org/10.1002/hyp.319>, 2001.
- Carey, S. K. and Woo, M.-K.: Hydrology of two slopes in subarctic Yukon, Canada, *Hydrol Process*, 13, 2549–2562, [https://doi.org/10.1002/\(SICI\)1099-1085\(199911\)13:16<2549::AID-HYP938>3.0.CO;2-H](https://doi.org/10.1002/(SICI)1099-1085(199911)13:16<2549::AID-HYP938>3.0.CO;2-H), 1999.
- Chen, R., Wang, G., Yang, Y., Liu, J., Han, C., Song, Y., Liu, Z., and Kang, E.: Effects of Cryospheric Change on Alpine Hydrology: Combining a Model With Observations in the Upper Reaches of the Hei River, China, *Journal of Geophysical Research: Atmospheres*, 123, 3414–3442, <https://doi.org/10.1002/2017JD027876>, 2018.
- Cheng, G. and Jin, H.: Permafrost and groundwater on the Qinghai-Tibet Plateau and in northeast China, *Hydrogeol J*, 21, 5–23, <https://doi.org/10.1007/s10040-012-0927-2>, 2013.
- a mis en forme** : Retrait : Suspendu : 0.75 cm, Espace Après : 3 pt
- a supprimé** : Aoya, M., Wallis, S. R., Terada, K., Lee, J., Kawakami, T., Wang, Y. and Heizler, M.: North-south extension in the Tibetan crust triggered by granite emplacement, *Geology*, 33(11), 853, doi:10.1130/G21806.1, 2005.¶
Bhattacharya, A., Bolch, T., Mukherjee, K., King, O., Menounos, B., Kapitsa, V., Neckel, N., Yang, W. and Yao, T.: High Mountain Asian glacier response to climate revealed by multi-temporal satellite observations since the 1960s, *Nat. Commun.*, 12(1), 4133, doi:10.1038/s41467-021-24180-y, 2021.¶
Bibi, S., Wang, L., Li, X., Zhou, J., Chen, D. and Yao, T.: Climatic and associated cryospheric, biospheric, and hydrological changes on the Tibetan Plateau: a review, *Int. J. Climatol.*, 38(January), e1–e17, doi:10.1002/joc.5411, 2018.¶
Biskop, S., Maussion, F., Krause, P. and Fink, M.: Differences in the water-balance components of four lakes in the southern-central Tibetan Plateau, *Hydrol. Earth Syst. Sci.*, 20(1), 209–225, doi:10.5194/hess-20-209-2016, 2016.¶
Bolch, T., Shea, J. M., Liu, S., Azam, F. M., Gao, Y., Gruber, S., Immerzeel, W. W., Kulkarni, A., Li, H., Tahir, A. A., Zhang, G. and Zhang, Y.: Status and Change of the Cryosphere in the Extended Hindu Kush Himalaya Region, in *The Hindu Kush Himalaya Assessment: Mountains, Climate Change, Sustainability and People*, edited by P. Wester, A. Mishra, A. Mukherji, and A. B. Shrestha, pp. 209–255, Springer International Publishing, Cham., 2019.¶
Bring, A., Fedorova, I., Dibike, Y., Hinzman, L., Mård, J., Mernild, S. H., Prowse, T., Semenova, O., Stuefer, S. L. and Woo, M. -K.: Arctic terrestrial hydrology: A synthesis of processes, regional effects, and research challenges, *J. Geophys. Res. Biogeosciences*, 121(3), 621–649, doi:10.1002/2015JG003131, 2016.¶
Brun, F., Berthier, E., Wagnon, P., Kääb, A. and Treichler, D.: A spatially resolved estimate of High Mountain Asia glacier mass balances from 2000 to 2016, *Nat. Geosci.*, 10(9), 668–673, doi:10.1038/ngeo2999, 2017.¶
Brun, F., Treichler, D., Shean, D. and Immerzeel, W. W.: Limited Contribution of Glacier Mass Loss to the Recent Increase in Tibetan Plateau Lake Volume, *Front. Earth Sci.*, 8(November), 1–14, doi:10.3389/feart.2020.582060, 2020.¶
Cao, J., Qin, D., Kang, E. and Li, Y.: River discharge changes in the Qinghai-Tibet Plateau, *Chinese Sci. Bull.*, 51(5), 594–600, doi:10.1007/s11434-006-0594-6, 2006.¶
Carey, S. K. and Woo, M.-K.: Hydrology of two slopes in subarctic Yukon, Canada, *Hydrol. Process.*, 13(16), 2549–2562, doi:10.1002/(SICI)1099-1085(199911)13:16<2549::AID-HYP938>3.0.CO;2-H, 1999.¶
Carey, S. K. and Woo, M.: Spatial variability of hillslope water balance, wolf creek basin, subarctic yukon, *Hydrol. Process.*, 15(16), 3113–3132, doi:10.1002/hyp.319, 2001.¶
Chen, R., Wang, G., Yang, Y., Liu, J., Han, C., Song, Y., Liu, Z. and Kang, E.: Effects of Cryospheric Change on Alpine Hydrology: Combining a Model With Observations in the Upper Reaches of the Hei River, China, *J. Geophys. Res. Atmos.*, 123(7), 3414–3442, doi:10.1002/2017JD027876, 2018.¶
Cheng, G. and Jin, H.: Permafrost and groundwater on the Qinghai-Tibet Plateau and in northeast China, *Hydrogeol. J.*, 21(1), 5–23, doi:10.1007/s10040-012-0927-2, 2013.¶
Cuo, L., Zhang, Y., Bohn, T. J., Zhao, L., Li, J., Liu, Q. and
- a mis en forme** : Centré, Retrait : Première ligne : 0 cm
- a mis en forme** : Police : 10 pt, Gras

- Cuo, L., Zhang, Y., Bohn, T. J., Zhao, L., Li, J., Liu, Q., and Zhou, B.: Frozen soil degradation and its effects on surface hydrology in the northern Tibetan Plateau, *Journal of Geophysical Research: Atmospheres*, 120, 8276–8298, <https://doi.org/10.1002/2015JD023193>, 2015.
- Dall'Amico, M., Endrizzi, S., Gruber, S., and Rigon, R.: A robust and energy-conserving model of freezing variably-saturated soil, *Cryosphere*, 5, 469–484, <https://doi.org/10.5194/tc-5-469-2011>, 2011.
- Ding, Y., Zhang, S., Chen, R., Han, T., Han, H., Wu, J., Li, X., Zhao, Q., Shangguan, D., Yang, Y., Liu, J., Wang, S., Qin, J., and Chang, Y.: Hydrological Basis and Discipline System of Cryohydrology: From a Perspective of Cryospheric Science, *Front Earth Sci (Lausanne)*, 8, 1–12, <https://doi.org/10.3389/feart.2020.574707>, 2020.
- Fiddes, J. and Gruber, S.: TopoSUB: A tool for efficient large area numerical modelling in complex topography at sub-grid scales, *Geosci Model Dev*, 5, 1245–1257, <https://doi.org/10.5194/gmd-5-1245-2012>, 2012.
- Fiddes, J. and Gruber, S.: TopoSCALE v.1.0: downscaling gridded climate data in complex terrain, *Geosci Model Dev*, 7, 387–405, <https://doi.org/10.5194/gmd-7-387-2014>, 2014.
- Fisher, J. P., Estop-Aragonés, C., Thierry, A., Charman, D. J., Wolfe, S. A., Hartley, I. P., Murton, J. B., Williams, M., and Phoenix, G. K.: The influence of vegetation and soil characteristics on active-layer thickness of permafrost soils in boreal forest, *Glob Chang Biol*, 22, 3127–3140, <https://doi.org/10.1111/gcb.13248>, 2016.
- Gao, B., Yang, D., Qin, Y., Wang, Y., Li, H., Zhang, Y., and Zhang, T.: Change in frozen soils and its effect on regional hydrology, upper Heihe basin, northeastern Qinghai-Tibetan Plateau, *Cryosphere*, 12, 657–673, <https://doi.org/10.5194/tc-12-657-2018>, 2018.
- Gao, H., Hrachowitz, M., Fenicia, F., Gharari, S., and Savenije, H. H. G.: Testing the realism of a topography-driven model (FLEX-Topo) in the nested catchments of the Upper Heihe, China, *Hydrol Earth Syst Sci*, 18, 1895–1915, <https://doi.org/10.5194/hess-18-1895-2014>, 2014.
- Gao, H., Wang, J., Yang, Y., Pan, X., Ding, Y., and Duan, Z.: Permafrost Hydrology of the Qinghai-Tibet Plateau: A Review of Processes and Modeling, *Front Earth Sci (Lausanne)*, 8, 1–13, <https://doi.org/10.3389/feart.2020.576838>, 2021.
- Gao, H., Han, C., Chen, R., Feng, Z., Wang, K., Fenicia, F., and Savenije, H.: Frozen soil hydrological modeling for a mountainous catchment northeast of the Qinghai-Tibet Plateau, *Hydrol Earth Syst Sci*, 26, 4187–4208, <https://doi.org/10.5194/hess-26-4187-2022>, 2022.
- Gao, H., Fenicia, F., and Savenije, H. H. G.: HESS Opinions: Are soils overrated in hydrology?, <https://doi.org/10.5194/egusphere-2023-125>, n.d.
- van Genuchten, M. Th.: A Closed-form Equation for Predicting the Hydraulic Conductivity of Unsaturated Soils, *Soil Science Society of America Journal*, 44, 892–898, <https://doi.org/10.2136/sssaj1980.03615995004400050002x>, 1980.
- Hersbach, H., Bell, B., Berrisford, P., Hirahara, S., Horányi, A., Muñoz-Sabater, J., Nicolas, J., Peubey, C., Radu, R., Schepers, D., Simmons, A., Soci, C., Abdalla, S., Abellan, X., Balsamo, G., Bechtold, P., Biavati, G., Bidlot, J., Bonavita, M., Chiara, G., Dahlgren, P., Dee, D., Diamantakis, M., Dragani, R., Flemming, J., Forbes, R., Fuentes, M., Geer, A., Haimberger, L., Healy, S., Hogan, R. J., Hólm, E., Janisková, M., Keeley, S., Laloyaux, P., Lopez, P., Lupu, C., Radnoti, G., Rosnay, P., Rozum, I., Vamborg, F., Villaume, S., and Thépaut, J.: The ERA5 global reanalysis, *Quarterly Journal of the Royal Meteorological Society*, 146, 1999–2049, <https://doi.org/10.1002/qj.3803>, 2020.
- Hu, G.-R., Li, X.-Y., and Yang, X.-F.: The impact of micro-topography on the interplay of critical zone architecture and hydrological processes at the hillslope scale: Integrated geophysical and hydrological experiments on the Qinghai-Tibet Plateau, *J Hydrol (Amst)*, 583, 124618, <https://doi.org/10.1016/j.jhydrol.2020.124618>, 2020.

a mis en forme : Centré, Retrait : Première ligne : 0 cm

a mis en forme : Police : 10 pt, Gras

- [Huang, K., Dai, J., Wang, G., Chang, J., Lu, Y., Song, C., Hu, Z., Ahmed, N., and Ye, R.: The impact of land surface temperatures on suprapermafrost groundwater on the central Qinghai-Tibet Plateau, *Hydrol Process*, 34, 1475–1488, <https://doi.org/10.1002/hyp.13677>, 2020.](#)
- [Hugonnet, R., McNabb, R., Berthier, E., Menounos, B., Nuth, C., Girod, L., Farinotti, D., Huss, M., Dussaillant, I., Brun, F., and Käab, A.: Accelerated global glacier mass loss in the early twenty-first century, *Nature*, 592, 726–731, <https://doi.org/10.1038/s41586-021-03436-z>, 2021.](#)
- [IPCC: IPCC Special Report on the Ocean and Cryosphere in a Changing Climate, Intergovernmental Panel on Climate Change, undefined, 2019.](#)
- [Jiang, H., Yang, Y., Bai, Y., and Wang, H.: Evaluation of the Total, Direct, and Diffuse Solar Radiations From the ERA5 Reanalysis Data in China, *IEEE Geoscience and Remote Sensing Letters*, 17, 47–51, <https://doi.org/10.1109/LGRS.2019.2916410>, 2020.](#)
- [Jiang, Q., Li, W., Fan, Z., He, X., Sun, W., Chen, S., Wen, J., Gao, J., and Wang, J.: Evaluation of the ERA5 reanalysis precipitation dataset over Chinese Mainland, *J Hydrol \(Amst\)*, 595, 125660, <https://doi.org/10.1016/j.jhydrol.2020.125660>, 2021.](#)
- [Jiao, D., Xu, N., Yang, F., and Xu, K.: Evaluation of spatial-temporal variation performance of ERA5 precipitation data in China, *Sci Rep*, 11, 17956, <https://doi.org/10.1038/s41598-021-97432-y>, 2021.](#)
- [Kampf, S. K.: Variability and persistence of hillslope initial conditions: A continuous perspective on subsurface flow response to rain events, *J Hydrol \(Amst\)*, 404, 176–185, <https://doi.org/10.1016/j.jhydrol.2011.04.028>, 2011.](#)
- [Kelleners, T. J., Chandler, D. G., McNamara, J. P., Gribb, M. M., and Seyfried, M. S.: Modeling Runoff Generation in a Small Snow-Dominated Mountainous Catchment, *Vadose Zone Journal*, 9, 517–527, <https://doi.org/10.2136/vzj2009.0033>, 2010.](#)
- [King, O., Bhattacharya, A., Bhambri, R., and Bolch, T.: Glacial lakes exacerbate Himalayan glacier mass loss, *Sci Rep*, 9, 18145, <https://doi.org/10.1038/s41598-019-53733-x>, 2019.](#)
- [Koren, V., Schaake, J., Mitchell, K., Duan, Q.-Y., Chen, F., and Baker, J. M.: A parameterization of snowpack and frozen ground intended for NCEP weather and climate models, *Journal of Geophysical Research: Atmospheres*, 104, 19569–19585, <https://doi.org/10.1029/1999JD900232>, 1999.](#)
- [Kurylyk, B. L., MacQuarrie, K. T. B., and McKenzie, J. M.: Climate change impacts on groundwater and soil temperatures in cold and temperate regions: Implications, mathematical theory, and emerging simulation tools, *Earth Sci Rev*, 138, 313–334, <https://doi.org/10.1016/j.earscirev.2014.06.006>, 2014.](#)
- [Lamontagne-Hallé, P., McKenzie, J. M., Kurylyk, B. L., and Zipper, S. C.: Changing groundwater discharge dynamics in permafrost regions, *Environmental Research Letters*, 13, 084017, <https://doi.org/10.1088/1748-9326/aad404>, 2018.](#)
- [Langer, M., Westermann, S., Boike, J., Kirillin, G., Grosse, G., Peng, S., and Krinner, G.: Rapid degradation of permafrost underneath waterbodies in tundra landscapes-Toward a representation of thermokarst in land surface models, *J Geophys Res Earth Surf*, 121, 2446–2470, <https://doi.org/10.1002/2016JF003956>, 2016.](#)
- [Lei, Y., Yao, T., Bird, B. W., Yang, K., Zhai, J., and Sheng, Y.: Coherent lake growth on the central Tibetan Plateau since the 1970s: Characterization and attribution, *J Hydrol \(Amst\)*, 483, 61–67, <https://doi.org/10.1016/j.jhydrol.2013.01.003>, 2013.](#)
- [Lei, Y., Yang, K., Wang, B., Sheng, Y., Bird, B. W., Zhang, G., and Tian, L.: Response of inland lake dynamics over the Tibetan Plateau to climate change, *Clim Change*, 125, 281–290, <https://doi.org/10.1007/s10584-014-1175-3>, 2014.](#)
- [Lei, Y., Yao, T., Yang, K., Bird, B. W., Tian, L., Zhang, X., Wang, W., Xiang, Y., Dai, Y., Lazhu, Zhou, J., and Wang, L.: An integrated investigation of lake storage and water level changes in the Paiku Co](#)

a mis en forme : Centré, Retrait : Première ligne : 0 cm

a mis en forme : Police : 10 pt, Gras

[basin, central Himalayas, J Hydrol \(Amst\), 562, 599–608,
https://doi.org/10.1016/j.jhydrol.2018.05.040, 2018.](#)

[Lei, Y., Yao, T., Yang, K., Ma, Y., and Bird, B. W.: Contrasting hydrological and thermal intensities determine seasonal lake-level variations – a case study at Paiku Co on the southern Tibetan Plateau, Hydrol Earth Syst Sci, 25, 3163–3177, <https://doi.org/10.5194/hess-25-3163-2021>, 2021.](#)

[Lei, Y., Yang, K., Immerzeel, W. W., Song, P., Bird, B. W., He, J., Zhao, H., and Li, Z.: Critical Role of Groundwater Inflow in Sustaining Lake Water Balance on the Western Tibetan Plateau, Geophys Res Lett, 49, <https://doi.org/10.1029/2022GL099268>, 2022.](#)

[Li, B., Yu, Z., Liang, Z., and Acharya, K.: Hydrologic response of a high altitude glacierized basin in the central Tibetan Plateau, Glob Planet Change, 118, 69–84, <https://doi.org/10.1016/j.gloplacha.2014.04.006>, 2014.](#)

[Li, D., Lu, X., Overeem, I., Walling, D. E., Syvitski, J., Kettner, A. J., Bookhagen, B., Zhou, Y., and Zhang, T.: Exceptional increases in fluvial sediment fluxes in a warmer and wetter High Mountain Asia, Science \(1979\), 374, 599–603, <https://doi.org/10.1126/science.abi9649>, 2021.](#)

[Li, H., Li, X., Yang, D., Wang, J., Gao, B., Pan, X., Zhang, Y., and Hao, X.: Tracing Snowmelt Paths in an Integrated Hydrological Model for Understanding Seasonal Snowmelt Contribution at Basin Scale, Journal of Geophysical Research: Atmospheres, 124, 8874–8895, <https://doi.org/10.1029/2019JD030760>, 2019.](#)

[Liefert, D. T., Shuman, B. N., Parsekian, A. D., and Mercer, J. J.: Why Are Some Rocky Mountain Lakes Ephemeral?, Water Resour Res, 54, 5245–5263, <https://doi.org/10.1029/2017WR022261>, 2018.](#)

[Luo, D., Jin, H., Wu, Q., Bense, V. F., He, R., Ma, Q., Gao, S., Jin, X., and Lü, L.: Thermal regime of warm-dry permafrost in relation to ground surface temperature in the Source Areas of the Yangtze and Yellow rivers on the Qinghai-Tibet Plateau, SW China, Science of the Total Environment, 618, 1033–1045, <https://doi.org/10.1016/j.scitotenv.2017.09.083>, 2018.](#)

[Luo, D., Jin, H., Bense, V. F., Jin, X., and Li, X.: Hydrothermal processes of near-surface warm permafrost in response to strong precipitation events in the Headwater Area of the Yellow River, Tibetan Plateau, Geoderma, 376, 114531, <https://doi.org/10.1016/j.geoderma.2020.114531>, 2020.](#)

[Magnin, F., Josnin, J.-Y., Ravel, L., Pergaud, J., Pohl, B., and Deline, P.: Modelling rock wall permafrost degradation in the Mont Blanc massif from the LIA to the end of the 21st century, Cryosphere, 11, 1813–1834, <https://doi.org/10.5194/tc-11-1813-2017>, 2017.](#)

[Martin, L. C. P., Nitzbon, J., Aas, K. S. S., Eitzelmüller, B., Kristiansen, H., and Westermann, S.: Stability Conditions of Peat Plateaus and Palsas in Northern Norway, J Geophys Res Earth Surf, 124, 705–719, <https://doi.org/10.1029/2018JF004945>, 2019.](#)

[Maurer, J. M., Schaefer, J. M., Rupper, S., and Corley, A.: Acceleration of ice loss across the Himalayas over the past 40 years, Sci Adv, 5, <https://doi.org/10.1126/sciadv.aav7266>, 2019.](#)

[McDonnell, J. J.: Are all runoff processes the same?, Hydrol Process, 27, 4103–4111, <https://doi.org/10.1002/hyp.10076>, 2013.](#)

[Mirus, B. B. and Loague, K.: How runoff begins \(and ends\): Characterizing hydrologic response at the catchment scale, Water Resour Res, 49, 2987–3006, <https://doi.org/10.1002/wrcr.20218>, 2013.](#)

[Monin, A. S. and Obukhov, A. M.: Basic laws of turbulent mixing in the surface layer of the atmosphere, Contrib. Geophys. Inst. Acad. Sci. USSR, 151, 163–187, 1954.](#)

[Mualem, Y.: A new model for predicting the hydraulic conductivity of unsaturated porous media, Water Resour Res, 12, 513–522, <https://doi.org/10.1029/WR012i003p00513>, 1976.](#)

[Nakano, Y. and Brown, J.: Mathematical Modeling and Validation of the Thermal Regimes in Tundra Soils, Barrow, Alaska, Arctic and Alpine Research, 4, 19, <https://doi.org/10.2307/1550211>, 1972.](#)

a mis en forme : Centré, Retrait : Première ligne : 0 cm

a mis en forme : Police : 10 pt, Gras

- Niu, L., Ye, B., Li, J., and Sheng, Y.: Effect of permafrost degradation on hydrological processes in typical basins with various permafrost coverage in Western China, *Sci China Earth Sci*, 54, 615–624, <https://doi.org/10.1007/s11430-010-4073-1>, 2011.
- Niu, L., Ye, B., Ding, Y., Li, J., Zhang, Y., Sheng, Y., and Yue, G.: Response of hydrological processes to permafrost degradation from 1980 to 2009 in the Upper Yellow River Basin, China, *Hydrology Research*, 47, 1014–1024, <https://doi.org/10.2166/nh.2016.096>, 2016.
- Obu, J., Westermann, S., Bartsch, A., Berdnikov, N., Christiansen, H. H., Dashtseren, A., Delaloye, R., Elberling, B., Etzelmüller, B., Kholodov, A., Khomutov, A., Kääh, A., Leibman, M. O., Lewkowitz, A. G., Panda, S. K., Romanovsky, V., Way, R. G., Westergaard-Nielsen, A., Wu, T., Yamkhin, J., and Zou, D.: Northern Hemisphere permafrost map based on TTOP modelling for 2000–2016 at 1 km² scale, *Earth Sci Rev*, 193, 299–316, <https://doi.org/10.1016/j.earscirev.2019.04.023>, 2019.
- Orsolini, Y., Wegmann, M., Dutra, E., Liu, B., Balsamo, G., Yang, K., de Rosnay, P., Zhu, C., Wang, W., Senan, R., and Arduini, G.: Evaluation of snow depth and snow cover over the Tibetan Plateau in global reanalyses using in situ and satellite remote sensing observations, *Cryosphere*, 13, 2221–2239, <https://doi.org/10.5194/tc-13-2221-2019>, 2019.
- Penman, H. L.: Natural evaporation from open water, bare soil and grass, *Proc R Soc Lond A Math Phys Sci*, 193, 120–145, 1948.
- Pepin, N., Bradley, R. S., Diaz, H. F., Baraer, M., Caceres, E. B., Forsythe, N., Fowler, H., Greenwood, G., Hashmi, M. Z., Liu, X. D., Miller, J. R., Ning, L., Ohmura, A., Palazzi, E., Rangwala, I., Schöner, W., Severskiy, I., Shahgedanova, M., Wang, M. B., Williamson, S. N., and Yang, D. Q.: Elevation-dependent warming in mountain regions of the world, *Nat Clim Chang*, 5, 424–430, <https://doi.org/10.1038/nclimate2563>, 2015.
- Pomeroy, J. W., Gray, D. M., Brown, T., Hedstrom, N. R., Quinton, W. L., Granger, R. J., and Carey, S. K.: The cold regions hydrological model: a platform for basing process representation and model structure on physical evidence, *Hydrol Process*, 21, 2650–2667, <https://doi.org/10.1002/hyp.6787>, 2007.
- Qiao, B., Zhu, L., and Yang, R.: Temporal-spatial differences in lake water storage changes and their links to climate change throughout the Tibetan Plateau, *Remote Sens Environ*, 222, 232–243, <https://doi.org/10.1016/j.rse.2018.12.037>, 2019.
- Qin, Y., Yang, D., Gao, B., Wang, T., Chen, J., Chen, Y., Wang, Y., and Zheng, G.: Impacts of climate warming on the frozen ground and eco-hydrology in the Yellow River source region, China, *Science of the Total Environment*, 605–606, 830–841, <https://doi.org/10.1016/j.scitotenv.2017.06.188>, 2017.
- Qin, Y., Chen, J., Yang, D., and Wang, T.: Estimating Seasonally Frozen Ground Depth From Historical Climate Data and Site Measurements Using a Bayesian Model, *Water Resour Res*, 54, 4361–4375, <https://doi.org/10.1029/2017WR022185>, 2018.
- Qin, Y., Wu, T., Zhang, P., Liu, W., Xue, S., and Guo, Z.: Spatiotemporal freeze–thaw variations over the Qinghai–Tibet Plateau 1981–2017 from reanalysis, *International Journal of Climatology*, 41, 1438–1454, <https://doi.org/10.1002/joc.6849>, 2021.
- Ran, Y., Li, X., and Cheng, G.: Climate warming over the past half century has led to thermal degradation of permafrost on the Qinghai–Tibet Plateau, *Cryosphere*, 12, 595–608, <https://doi.org/10.5194/tc-12-595-2018>, 2018.
- RGI Consortium: Randolph Glacier Inventory - A Dataset of Global Glacier Outlines, Version 6, 2017.
- Richards, L. A.: CAPILLARY CONDUCTION OF LIQUIDS THROUGH POROUS MEDIUMS, *Physics* (College Park Md), 1, 318–333, <https://doi.org/10.1063/1.1745010>, 1931.
- Richardson, L. F.: Weather Prediction by Numerical Process, Cambridge University Press, 1922.

a mis en forme : Centré, Retrait : Première ligne : 0 cm

a mis en forme : Police : 10 pt, Gras

- Rosenberry, D. O., Lewandowski, J., Meinikmann, K., and Nützmann, G.: Groundwater - the disregarded component in lake water and nutrient budgets. Part 1: effects of groundwater on hydrology, *Hydrol Process*, 29, 2895–2921, <https://doi.org/10.1002/hyp.10403>, 2015.
- Samuel, J. M., Sivapalan, M., and Struthers, I.: Diagnostic analysis of water balance variability: A comparative modeling study of catchments in Perth, Newcastle, and Darwin, Australia, *Water Resour Res*, 44, <https://doi.org/10.1029/2007WR006694>, 2008.
- Savenije, H. H. G.: HESS opinions “topography driven conceptual modelling (FLEX-Topo),” *Hydrol Earth Syst Sci*, 14, 2681–2692, <https://doi.org/10.5194/hess-14-2681-2010>, 2010.
- Searle, M. P., Parrish, R. R., Hodges, K. V., Hurford, A., Ayres, M. W., and Whitehouse, M. J.: Shisha Pangma Leucogranite, South Tibetan Himalaya: Field Relations, Geochemistry, Age, Origin, and Emplacement, *J Geol*, 105, 295–318, <https://doi.org/10.1086/515924>, 1997.
- Seibert, J., Rodhe, A., and Bishop, K.: Simulating interactions between saturated and unsaturated storage in a conceptual runoff model, *Hydrol Process*, 17, 379–390, <https://doi.org/10.1002/hyp.1130>, 2003.
- Shaman, J., Stieglitz, M., Engel, V., Koster, R., and Stark, C.: Representation of subsurface storm flow and a more responsive water table in a TOPMODEL-based hydrology model, *Water Resour Res*, 38, 31-1-31–16, <https://doi.org/10.1029/2001wr000636>, 2002.
- Shangguan, W., Dai, Y., Liu, B., Zhu, A., Duan, Q., Wu, L., Ji, D., Ye, A., Yuan, H., Zhang, Q., Chen, D., Chen, M., Chu, J., Dou, Y., Guo, J., Li, H., Li, J., Liang, L., Liang, X., Liu, H., Liu, S., Miao, C., and Zhang, Y.: A China data set of soil properties for land surface modeling, *J Adv Model Earth Syst*, 5, 212–224, <https://doi.org/10.1002/jame.20026>, 2013.
- Shangguan, W., Hengl, T., Mendes de Jesus, J., Yuan, H., and Dai, Y.: Mapping the global depth to bedrock for land surface modeling, *J Adv Model Earth Syst*, 9, 65–88, <https://doi.org/10.1002/2016MS000686>, 2017.
- Shean, D. E., Bhushan, S., Montesano, P., Rounce, D. R., Arendt, A., and Osmanoglu, B.: A Systematic, Regional Assessment of High Mountain Asia Glacier Mass Balance, *Front Earth Sci (Lausanne)*, 7, 1–19, <https://doi.org/10.3389/feart.2019.00363>, 2020.
- Sjöberg, Y., Jan, A., Painter, S. L., Coon, E. T., Carey, M. P., O’Donnell, J. A., and Koch, J. C.: Permafrost Promotes Shallow Groundwater Flow and Warmer Headwater Streams, *Water Resour Res*, 57, 1–20, <https://doi.org/10.1029/2020WR027463>, 2021.
- Song, L., Wang, L., Li, X., Zhou, J., Luo, D., Jin, H., Qi, J., Zeng, T., and Yin, Y.: Improving Permafrost Physics in a Distributed Cryosphere-Hydrology Model and Its Evaluations at the Upper Yellow River Basin, *Journal of Geophysical Research: Atmospheres*, 125, 1–22, <https://doi.org/10.1029/2020JD032916>, 2020.
- Themeßl, M. J., Gobiet, A., and Leuprecht, A.: Empirical-statistical downscaling and error correction of daily precipitation from regional climate models, *International Journal of Climatology*, 31, 1530–1544, <https://doi.org/10.1002/joc.2168>, 2011.
- Vionnet, V., Brun, E., Morin, S., Boone, A., Faroux, S., Le Moigne, P., Martin, E., and Willemet, J.-M.: The detailed snowpack scheme Crocus and its implementation in SURFEX v7.2, *Geosci Model Dev*, 5, 773–791, <https://doi.org/10.5194/gmd-5-773-2012>, 2012.
- Vörösmarty, C. J., Moore, B., Grace, A. L., Gildea, M. P., Melillo, J. M., Peterson, B. J., Rastetter, E. B., and Steudler, P. A.: Continental scale models of water balance and fluvial transport: An application to South America, *Global Biogeochem Cycles*, 3, 241–265, <https://doi.org/10.1029/GB003i003p00241>, 1989.
- Walvoord, M. A. and Kurylyk, B. L.: Hydrologic Impacts of Thawing Permafrost—A Review, *Vadose Zone Journal*, 15, 0, <https://doi.org/10.2136/vzj2016.01.0010>, 2016.

a mis en forme : Centré, Retrait : Première ligne : 0 cm

a mis en forme : Police : 10 pt, Gras

- Wang, C., Zhao, W., and Cui, Y.: Changes in the Seasonally Frozen Ground Over the Eastern Qinghai-Tibet Plateau in the Past 60 Years Characteristics of Seasonally Frozen, 8, 1–11, <https://doi.org/10.3389/feart.2020.00270>, 2020a.
- Wang, G., Li, Y., Hu, H., and Wang, Y.: Synergistic effect of vegetation and air temperature changes on soil water content in alpine frost meadow soil in the permafrost region of Qinghai-Tibet, *Hydrol Process*, 22, 3310–3320, <https://doi.org/10.1002/hyp.6913>, 2008.
- Wang, G., Lin, S., Hu, Z., Lu, Y., Sun, X., and Huang, K.: Improving Actual Evapotranspiration Estimation Integrating Energy Consumption for Ice Phase Change Across the Tibetan Plateau, *Journal of Geophysical Research: Atmospheres*, 125, 1–13, <https://doi.org/10.1029/2019JD031799>, 2020b.
- Wang, L., Yi, C., Xu, X., Schütt, B., Liu, K., and Zhou, L.: Soil properties in two soil profiles from terraces of the Nam Co Lake in Tibet, China, *J Mt Sci*, 6, 354–361, <https://doi.org/10.1007/s11629-009-1017-3>, 2009.
- Wang, Q., Fan, X., and Wang, M.: Recent warming amplification over high elevation regions across the globe, *Clim Dyn*, 43, 87–101, <https://doi.org/10.1007/s00382-013-1889-3>, 2014.
- Wang, X. and Gao, B.: Frozen soil change and its impact on hydrological processes in the Qinghai Lake Basin, the Qinghai-Tibetan Plateau, China, *J Hydrol Reg Stud*, 39, 100993, <https://doi.org/10.1016/j.ejrh.2022.100993>, 2022.
- Wang, Y., Yang, H., Gao, B., Wang, T., Qin, Y., and Yang, D.: Frozen ground degradation may reduce future runoff in the headwaters of an inland river on the northeastern Tibetan Plateau, *J Hydrol (Amst)*, 564, 1153–1164, <https://doi.org/10.1016/j.jhydrol.2018.07.078>, 2018.
- Watras, C. J., Read, J. S., Holman, K. D., Liu, Z., Song, Y.-Y., Watras, A. J., Morgan, S., and Stanley, E. H.: Decadal oscillation of lakes and aquifers in the upper Great Lakes region of North America: Hydroclimatic implications, *Geophys Res Lett*, 41, 456–462, <https://doi.org/10.1002/2013GL058679>, 2014.
- Westermann, S., Schuler, T. V., Gislén, K., and Eitzelmüller, B.: Transient thermal modeling of permafrost conditions in Southern Norway, *Cryosphere*, 7, 719–739, <https://doi.org/10.5194/tc-7-719-2013>, 2013.
- Westermann, S., Langer, M., Boike, J., Heikenfeld, M., Peter, M., Eitzelmüller, B., and Krinner, G.: Simulating the thermal regime and thaw processes of ice-rich permafrost ground with the land-surface model CryoGrid 3, *Geosci Model Dev*, 9, 523–546, <https://doi.org/10.5194/gmd-9-523-2016>, 2016.
- Westermann, S., Ingeman-Nielsen, T., Scheer, J., Aalstad, K., Aga, J., Chaudhary, N., Eitzelmüller, B., Filhol, S., Kääh, A., Renette, C., Schmidt, L. S., Schuler, T. V., Zweigel, R. B., Martin, L., Morard, S., Ben-Asher, M., Angelopoulos, M., Boike, J., Groenke, B., Miesner, F., Nitzbon, J., Overduin, P., Stuenzi, S. M., and Langer, M.: The CryoGrid community model (version 1.0) – a multi-physics toolbox for climate-driven simulations in the terrestrial cryosphere, *Geosci Model Dev*, 16, 2607–2647, <https://doi.org/10.5194/gmd-16-2607-2023>, 2023.
- Wu, Q. and Zhang, T.: Recent permafrost warming on the Qinghai-Tibetan Plateau, *J Geophys Res*, 113, D13108, <https://doi.org/10.1029/2007JD009539>, 2008.
- Wünnemann, B., Yan, D., and Ci, R.: Morphodynamics and lake level variations at Paiku Co, southern Tibetan Plateau, China, *Geomorphology*, 246, 489–501, <https://doi.org/10.1016/j.geomorph.2015.07.007>, 2015.
- Yang, K., Wu, H., Qin, J., Lin, C., Tang, W., and Chen, Y.: Recent climate changes over the Tibetan Plateau and their impacts on energy and water cycle: A review, *Glob Planet Change*, 112, 79–91, <https://doi.org/10.1016/j.gloplacha.2013.12.001>, 2014a.
- Yang, K., Wang, J., Lei, Y., Chen, Y., Zhu, L., Ding, B., and Qin, J.: Quantifying evaporation and its decadal change for Lake Nam Co, central Tibetan Plateau, *Journal of Geophysical Research: Atmospheres*, 121, 7578–7591, <https://doi.org/10.1002/2015JD024523>, 2016.

a mis en forme : Centré, Retrait : Première ligne : 0 cm

a mis en forme : Police : 10 pt, Gras

- Yang, S., Zhang, H., Kong, M., Liu, Y., Liu, H., and Xu, R.: Study on surficial soil geochemistry in the high-elevation and-frigid mountainous region: A case of Qulong porphyry copper deposit in Tibet, J Geochem Explor, 139, 144–151, <https://doi.org/10.1016/j.gexplo.2013.06.001>, 2014b.
- Yang, Y., Wu, Q., Jin, H., Wang, Q., Huang, Y., Luo, D., Gao, S., and Jin, X.: Delineating the hydrological processes and hydraulic connectivities under permafrost degradation on Northeastern Qinghai-Tibet Plateau, China, J Hydrol (Amst), 569, 359–372, <https://doi.org/10.1016/j.jhydrol.2018.11.068>, 2019.
- Yao, F., Wang, J., Yang, K., Wang, C., Walter, B. A., and Crétaux, J.-F.: Lake storage variation on the endorheic Tibetan Plateau and its attribution to climate change since the new millennium, Environmental Research Letters, 13, 064011, <https://doi.org/10.1088/1748-9326/aab5d3>, 2018.
- Yecheili, Y., Ronen, D., Berkowitz, B., Dershowitz, W. S., and Hadad, A.: Aquifer Characteristics Derived From the Interaction Between Water Levels of a Terminal Lake (Dead Sea) and an Adjacent Aquifer, Water Resour Res, 31, 893–902, <https://doi.org/10.1029/94WR03154>, 1995.
- Yi, S., Arain, M. A., and Woo, M.-K.: Modifications of a land surface scheme for improved simulation of ground freeze-thaw in northern environments, Geophys Res Lett, 33, L13501, <https://doi.org/10.1029/2006GL026340>, 2006.
- Yuan, Z., Jin, H., Wang, Q., Wu, Q., Li, G., Jin, X., and Ma, Q.: Profile distributions of soil organic carbon fractions in a permafrost region of the Qinghai–Tibet Plateau, Permafrost Periglacial Process, 31, 538–547, <https://doi.org/10.1002/ppp.2055>, 2020.
- Zhang, G., Yao, T., Piao, S., Bolch, T., Xie, H., Chen, D., Gao, Y., O'Reilly, C. M., Shum, C. K., Yang, K., Yi, S., Lei, Y., Wang, W., He, Y., Shang, K., Yang, X., and Zhang, H.: Extensive and drastically different alpine lake changes on Asia's high plateaus during the past four decades, Geophys Res Lett, 44, 252–260, <https://doi.org/10.1002/2016GL072033>, 2017.
- Zhang, G., Nan, Z., Wu, X., Ji, H., and Zhao, S.: The Role of Winter Warming in Permafrost Change Over the Qinghai-Tibet Plateau, Geophys Res Lett, 46, 11261–11269, <https://doi.org/10.1029/2019GL084292>, 2019.
- Zhang, G., Yao, T., Xie, H., Yang, K., Zhu, L., Shum, C. K., Bolch, T., Yi, S., Allen, S., Jiang, L., Chen, W., and Ke, C.: Response of Tibetan Plateau lakes to climate change: Trends, patterns, and mechanisms, Earth Sci Rev, 208, 103269, <https://doi.org/10.1016/j.earscirev.2020.103269>, 2020a.
- Zhang, G., Bolch, T., Chen, W., and Crétaux, J.-F.: Comprehensive estimation of lake volume changes on the Tibetan Plateau during 1976–2019 and basin-wide glacier contribution, Science of The Total Environment, 772, 145463, <https://doi.org/10.1016/j.scitotenv.2021.145463>, 2021a.
- Zhang, G., Nan, Z., Zhao, L., Liang, Y., and Cheng, G.: Qinghai-Tibet Plateau wetting reduces permafrost thermal responses to climate warming, Earth Planet Sci Lett, 562, 116858, <https://doi.org/10.1016/j.epsl.2021.116858>, 2021b.
- Zhang, H., Immerzeel, W. W., Zhang, F., de Kok, R. J., Chen, D., and Yan, W.: Snow cover persistence reverses the altitudinal patterns of warming above and below 5000 m on the Tibetan Plateau, Science of The Total Environment, 803, 149889, <https://doi.org/10.1016/j.scitotenv.2021.149889>, 2022.
- Zhang, X., Wang, R., Yao, Z., and Liu, Z.: Variations in glacier volume and snow cover and their impact on lake storage in the Paiku Co Basin, in the Central Himalayas, Hydrol Process, 34, 1920–1933, <https://doi.org/10.1002/hyp.13703>, 2020b.
- Zhang, Y., Ohata, T., and Kadota, T.: Land-surface hydrological processes in the permafrost region of the eastern Tibetan Plateau, J Hydrol (Amst), 283, 41–56, [https://doi.org/10.1016/S0022-1694\(03\)00240-3](https://doi.org/10.1016/S0022-1694(03)00240-3), 2003.
- Zhong, X., Wang, L., Zhou, J., Li, X., Qi, J., Song, L., and Wang, Y.: Precipitation Dominates Long-Term Water Storage Changes in Nam Co Lake (Tibetan Plateau) Accompanied by Intensified Cryosphere

a mis en forme : Centré, Retrait : Première ligne : 0 cm

a mis en forme : Police : 10 pt, Gras

Melts Revealed by a Basin-Wide Hydrological Modelling, Remote Sens (Basel), 12, 1926, <https://doi.org/10.3390/rs12121926>, 2020.

Zhou, J., Wang, L., Zhang, Y., Guo, Y., Li, X., and Liu, W.: Exploring the water storage changes in the largest lake (Selin Co) over the Tibetan Plateau during 2003–2012 from a basin-wide hydrological modeling, Water Resour Res, 51, 8060–8086, <https://doi.org/10.1002/2014WR015846>, 2015.

Zou, D., Zhao, L., Sheng, Y., Chen, J., Hu, G., Wu, T., Wu, J., Xie, C., Wu, X., Pang, Q., Wang, W., Du, E., Li, W., Liu, G., Li, J., Qin, Y., Qiao, Y., Wang, Z., Shi, J., and Cheng, G.: A new map of permafrost distribution on the Tibetan Plateau, Cryosphere, 11, 2527–2542, <https://doi.org/10.5194/tc-11-2527-2017>, 2017.

Zweigel, R. B., Westermann, S., Nitzbon, J., Langer, M., Boike, J., Eitzelmüller, B., and Vikhamar Schuler, T.: Simulating Snow Redistribution and its Effect on Ground Surface Temperature at a High-Arctic Site on Svalbard, J Geophys Res Earth Surf, 126, 1–21, <https://doi.org/10.1029/2020JF005673>, 2021.

a mis en forme : Gauche, Espace Après : 0.6 ligne, Éviter veuves et orphelines, Espacement automatique entre les caractères asiatiques et latins, Espacement automatique entre les caractères asiatiques et les chiffres

a mis en forme : Police : 11 pt, Néerlandais (Pays-Bas)

a mis en forme : Centré, Retrait : Première ligne : 0 cm

a mis en forme : Police : 10 pt, Gras